

Degeneracy-Resilient Teach and Repeat for Geometrically Challenging Environments Using FMCW Lidar

Katya M. Papais*, Wenda Zhao*, Timothy D. Barfoot

Abstract—Teach and Repeat (T&R) topometric navigation enables robots to autonomously repeat previously traversed paths without relying on GPS, making it well suited for operations in GPS-denied environments such as underground mines and lunar navigation. State-of-the-art T&R systems typically rely on iterative closest point (ICP)-based estimation; however, in geometrically degenerate environments with sparsely structured terrain, ICP often becomes ill-conditioned, resulting in degraded localization and unreliable navigation performance. To address this challenge, we present a degeneracy-resilient Frequency-Modulated Continuous-Wave (FMCW) lidar T&R navigation system consisting of Doppler velocity-based odometry and degeneracy-aware scan-to-map localization. Leveraging FMCW lidar, which provides per-point radial velocity measurements via the Doppler effect, we extend a geometry-independent, correspondence-free motion estimation to include principled pose uncertainty estimation that remains stable in degenerate environments. We further propose a degeneracy-aware localization method that incorporates per-point curvature for improved data association, and unifies translational and rotational scales to enable consistent degeneracy detection. Closed-loop field experiments across three environments with varying structural richness demonstrate that the proposed system reliably completes autonomous navigation, including in a challenging flat airport test field where a conventional ICP-based system fails.

Index Terms—Field Robots, Localization, State Estimation, Optimization

I. INTRODUCTION

AUTONOMOUS navigation in GPS-denied environments, such as underground mines, tunnels, and planetary surfaces, often requires reliable localization without external positioning infrastructure [1]–[4]. In many scenarios, robots are required to perform repeated traversals for cargo transport or inspection between known locations [5]–[8], motivating navigation frameworks that emphasize repeatability, robustness, and efficiency. Teach and Repeat (T&R) topometric navigation is well suited to this setting, as it enables reliable, repeated autonomous traversal of previously driven routes after a single demonstration [9], [10]. By leveraging local submaps constructed during a previously driven path, T&R avoids the need for global mapping or online terrain assessment and provides consistent path execution, which is especially valuable in GPS-denied and infrastructure-free environments.

Light Detection and Ranging (lidar) sensors have proven to be a reliable sensing modality due to their high resolution, accurate range measurements, and invariance to lighting conditions, making Lidar Teach and Repeat (LT&R) systems

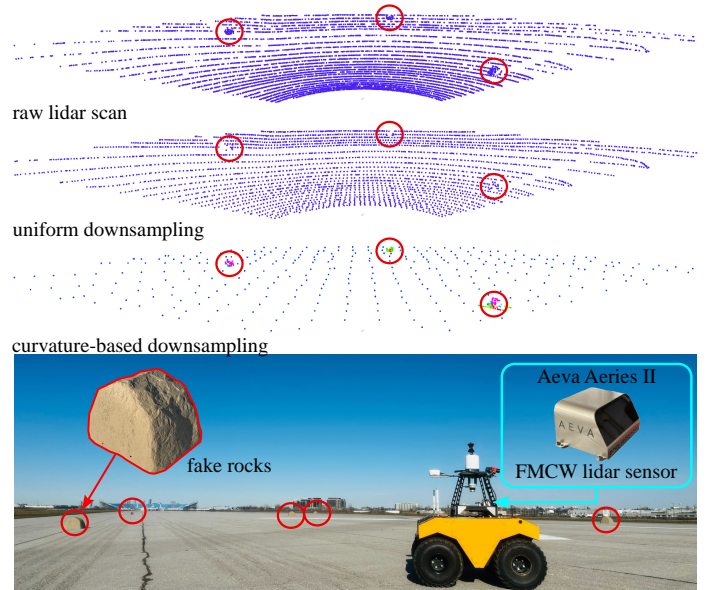


Fig. 1: Our proposed degeneracy-resilient FMCW Lidar Teach-and-Repeat (LT&R) system operating in a flat airport test field. The top image shows the raw lidar scan, followed by uniformly downsampled and curvature-based downsampled scans (coloured by curvature, where non-planar features are highlighted in different colours). In contrast to uniform downsampling, which treats all points equally and often discards sparse geometric features, curvature-based downsampling selectively reduces flat surfaces and preserves informative geometry, improving computational efficiency and the reliability of scan-to-map data association in geometrically degenerate environments. Fake rocks, circled in red, are added to the scene to introduce minimal geometric structure.

widely adopted for various applications [11]–[13]. State-of-the-art (SOTA) lidar-based estimation is often achieved by geometrically aligning lidar point clouds through an iterative process of nearest-neighbour data association, known as iterative closest point (ICP)-based methods [14], [15]. However, many GPS-denied environments, such as flat deserts, open fields, or planetary surfaces, often exhibit large-scale flat and sparsely structured regions, where geometric features are insufficient to fully constrain vehicle motion. In such environments, lidar-based localization methods that rely on ICP registration are prone to geometric degeneracy, leading to unreliable data association and degraded pose estimation. This challenge fundamentally limits the robustness of existing LT&R systems in geometrically degenerate scenarios.

Emerging lidar modalities, such as Frequency-Modulated Continuous Wave (FMCW) lidar, address this limitation by providing additional motion measurements that are less dependent on geometric structure. This sensing capability has

* Denotes equal contribution.

The authors are with the Institute for Aerospace Studies, University of Toronto, Canada.

been explored for precise navigation and soft-landing missions on planetary bodies, such as in the Autonomous Landing and Hazard Avoidance (ALHAT) project [16], [17]. FMCW lidar employs frequency-domain modulation to estimate range from beat frequency and directly measure per-point radial velocity via the Doppler effect [18]–[20]. These Doppler velocity measurements provide motion information that is particularly valuable in non-distinctive or repetitive environments with insufficient geometric constraints. Consequently, FMCW lidar, also referred to as Doppler lidar, has recently been adopted for Doppler-enhanced lidar odometry in autonomous driving, particularly in scenarios with weak or repetitive geometric structure such as tunnels, highways, and bridges [21]–[23].

While Doppler-based odometry provides reliable motion estimates in geometrically degenerate environments, T&R navigational frameworks require localization relative to the taught path to correct accumulated drift [10]. In lidar-based systems, this is typically accomplished through scan-to-map registration, which geometrically aligns incoming scans to a locally consistent map. In environments with limited structural variation, however, ICP-based registration becomes ill-conditioned due to insufficient geometric constraints, resulting in unreliable data association and drift along degenerate directions [24]–[26]. Improving the robustness of scan-to-map localization under such conditions is therefore critical for reliable navigation.

In this paper, we present a degeneracy-resilient FMCW LT&R navigation system. We first extend a Doppler velocity-based correspondence-free lidar-inertial odometry with pose uncertainty estimation, enabling uncertainty propagation from odometry into the localization process. To improve scan-to-map localization robustness and efficiency, we propose a curvature-enhanced, degeneracy-aware ICP localization algorithm that leverages per-point curvature for improved data association, and unifies translational and rotational scales to enable more reliable identification of degenerate directions. The proposed FMCW LT&R system is evaluated in closed-loop field experiments across three environments ranging from geometrically feature-rich to feature-limited scenarios. In particular, the full system successfully completes autonomous navigation in a flat airport test field (see Figure 1) where a conventional ICP-based LT&R system and partially ablated variants fail. Our contributions can be summarized as follows:

- We extend a Doppler velocity-based, correspondence-free lidar-inertial odometry framework with pose uncertainty estimation, enabling principled propagation of odometry uncertainty into subsequent localization.
- We propose a curvature-enhanced, degeneracy-aware ICP algorithm that incorporates per-point curvature information for improved data association and unifies translational and rotational scales to enable consistent degeneracy detection.
- We validate the proposed FMCW LT&R system in closed-loop field experiments across three environments ranging from feature-rich to feature-limited scenarios, and release the implementation to the community.

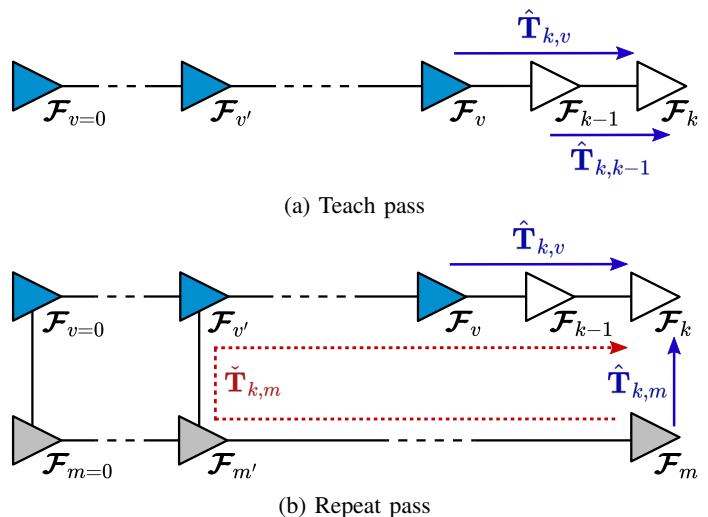


Fig. 2: Structure of the Teach-and-Repeat (T&R) pose graph during (a) the teach pass and (b) the repeat pass. \mathcal{F}_k denotes the current robot frame while \mathcal{F}_v and \mathcal{F}_m indicate the vertex frame from the current pass (teach or repeat), and the local submap frame from the reference (teach) pass, respectively. During both teach and repeat passes, the transformation $\hat{\mathbf{T}}_{k,v}$ from the latest vertex frame \mathcal{F}_v to the robot frame \mathcal{F}_k is estimated using odometry. During the repeat pass, $\mathcal{F}_{v'}$ denotes the most recently localized vertex against the reference vertex $\mathcal{F}_{m'}$. A prior for $\mathbf{T}_{k,m}$ is obtained by compounding transformations through \mathcal{F}_m , $\mathcal{F}_{v'}$, \mathcal{F}_v , and is refined via scan-to-map localization.

II. RELATED WORK

A. Teach and Repeat Topometric Navigation

T&R navigation is a topometric framework that enables reliable path following by reusing prior driving experience rather than constructing a globally consistent map [9]. During the teach phase (see Figure 2a), the robot traverses a desired route while building a graph of locally consistent submaps. During the repeat phase, the robot localizes against these submaps to estimate its pose relative to the taught path (as shown in Figure 2b) and track the demonstrated path. By performing localization in local reference frames, T&R avoids global consistency requirements and remains scalable over long distances [10].

A variety of sensing modalities have been explored within the T&R navigation framework. Early work primarily relied on cameras for metric localization, leading to the widely studied Visual Teach and Repeat (VT&R) paradigm [9], [27], [28]. However, the T&R framework generalizes beyond vision, and similar systems have been demonstrated using lidar [1], [11], [12], sonar [29], and radar [30]. Among these modalities, LT&R has attracted increasing attention due to its ability to provide accurate geometric measurements that support reliable localization across diverse operational conditions. As a result, LT&R has been widely adopted in applications such as off-road robotics [12], mining [1], agriculture [11], and planetary rover analogs [13], where reliable repeated traversal between known locations is required in large-scale and unstructured environments.

B. Lidar-based Point Cloud Registration

Lidar-based navigation systems commonly rely on point cloud registration for motion estimation. Registration between consecutive scans, commonly referred to as scan-to-scan registration, primarily provides an odometry estimate. In contrast, scan-to-map registration aligns incoming scans to a locally or globally maintained map and plays a critical role in localization by correcting accumulated odometry drift.

Among the many point-cloud registration techniques proposed in the literature, the ICP algorithm remains the most widely adopted approach for lidar-based registration [15]. ICP iteratively estimates the rigid-body transformation between a source and a target point cloud by alternating between nearest-neighbour data association and geometric alignment [14], [31]. A variety of cost functions have been explored, including point-to-point [14], point-to-line [32], point-to-plane [33], and plane-to-plane [34]. Other works investigate hybrid, statistically motivated, and certifiable optimization-based formulations [35]–[37]. Despite these alternatives, the point-to-plane cost function [38] remains a preferred choice in many SOTA lidar-based navigation systems due to its simplicity, robustness, and strong empirical performance in real-world deployments [2], [39], [40].

The performance of ICP-based registration is strongly influenced by data preprocessing, correspondence quality, and the geometric structure of the point cloud. Standard pipelines typically apply voxel-grid downsampling, normal estimation, and outlier filtering prior to registration [14], [15], [33]. While voxel downsampling effectively reduces computational cost [41], its uniform spatial treatment can disproportionately preserve large planar regions while removing fine geometric details (see Figure 1, uniform downsampling), which may degrade registration performance in environments with limited structural diversity.

Several works have emphasized that not all points contribute equally to robust registration. Feature-aware preprocessing and data association strategies have been proposed. Systems such as LOAM [42] and its successors, LeGO-LOAM [43] and F-LOAM [44], extract edge and planar points using a local-smoothness score computed along a scan ring, and use different voxel resolutions for the two classes. Surfel-based approaches, such as SuMa [45] and SuMa++ [46], similarly exploit local normal variation to guide data association. Beyond first-order geometric features, higher-order surface information has also been explored to capture more subtle shape variations. Quadratic surface fitting has been widely used to estimate local curvature, providing a richer description of local geometry [47]–[49]. Gaussian curvature has also been explored within ICP pipelines to assist point selection and correspondence filtering, leveraging its invariance under rigid transformations [50], [51]. These studies demonstrate that geometry-aware preprocessing and data association can improve the robustness of lidar-based point cloud registration, particularly in geometrically non-distinctive or repetitive environments.

Our method differs from prior curvature-based approaches in two main aspects. First, we cluster points into regions

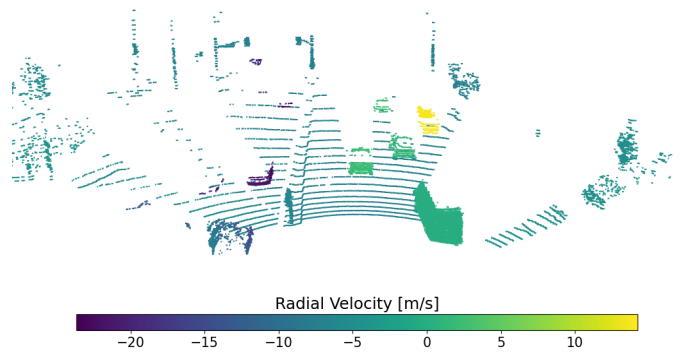


Fig. 3: Example FMCW lidar scan with points coloured by per-point radial velocity in the lidar frame. Lighter colours indicate positive radial velocity (moving away from the sensor), while darker colours indicate negative radial velocity (moving toward the sensor).

of similar curvature and apply separate downsampling to high- and low-curvature clusters, yielding more robust feature preservation in large-scale, geometrically degenerate environments. Second, whereas [50] relies on RANSAC-based correspondence selection using curvature similarity, we introduce a joint spatial–curvature correspondence metric for ICP registration, which resolves ambiguities in planar or repetitive regions without random sampling (see Figure 1, curvature-based downsampling).

C. FMCW Lidar Odometry

Recent advances in lidar technology have led to the emergence of FMCW lidar sensors, which provide dense 3D point clouds comparable to conventional time-of-flight lidar while additionally measuring per-point relative radial velocity via the Doppler effect [18], [19], [52]. Figure 3 illustrates an example FMCW lidar point cloud coloured by the Doppler velocity of each point. These properties have motivated growing interest in Doppler velocity-enhanced lidar odometry, particularly in scenarios with weak or repetitive geometric structure, such as tunnels, highways, and bridges.

Hexsel et al. introduced Doppler-ICP (DICP) [21], demonstrating that Doppler measurements can be integrated into ICP-based odometry to better constrain motion in environments where geometry alone is insufficient. Zhao et al. [53] integrate Doppler velocity measurements into a lidar–inertial ICP framework to leverage complementary sensing modalities, while Pang et al. [54] improve computational efficiency through scan-slicing strategies. Wu et al. [22] proposed a continuous-time formulation that directly incorporates Doppler measurements, removing the need for external motion compensation during preprocessing. Building on this idea, Yoon *et al.* [23] showed that data association between point clouds can be eliminated entirely with a lightweight, correspondence-free Doppler lidar-inertial odometry formulation. By avoiding nearest-neighbour association and explicit geometric matching, this approach is particularly well suited to environments with weak or repetitive geometric structure. Quantitative results show that their method is significantly faster than SOTA ICP-based odometry while being reasonably accurate.

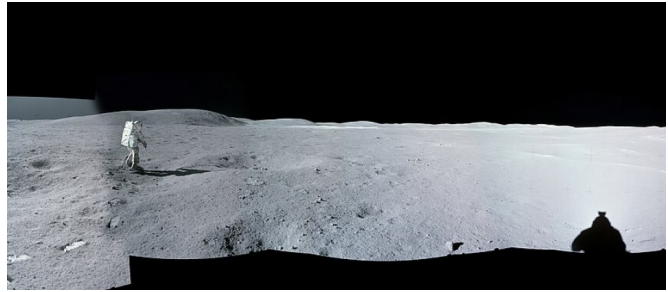
Despite these promising results, the correspondence-free Doppler lidar odometry method proposed by Yoon *et al.* primarily focuses on efficient motion estimation and does not explicitly model or propagate pose uncertainty. Consequently, while the method provides fast and robust odometry estimates in geometrically challenging environments, uncertainty information is not available for subsequent localization or optimization stages, limiting its direct integration into uncertainty-aware navigation frameworks.

D. Localization in Geometrically Degenerate Environments

There is growing interest in the robotics community in extending robotic systems to operate reliably in challenging, unstructured environments [2], [55], [56]. As robots operate in such settings, they inevitably encounter extreme environments characterized by non-distinctive or repetitive geometric structure, which pose significant challenges for lidar ICP-based navigation systems. Since ICP-based pose estimation is inherently unreliable in environments with non-distinctive or repetitive geometric structure, current solutions often rely on multi-sensor fusion [57]–[59] or the incorporation of complementary information to mitigate lidar degeneracy [60], [61]. Researchers have also looked into applying adaptive M-estimators [62], better feature sampling [63], [64], and adaptive matching techniques [65] to improve robustness of ICP performance. In the autonomous driving literature, dominant ground-plane structures are often explicitly segmented [66]–[68] to improve remote obstacle detection [69], [70] and ICP-based point cloud registration [71], [72]. However, such strategies typically rely on environment-specific assumptions and are not generally applicable, nor do they fully resolve the underlying optimization degeneracy caused by insufficient geometric constraints. Consequently, mitigating the impact of geometric degeneracy on ICP optimization remains fundamentally important for achieving degeneracy-resilient lidar-based navigation in the field.

The degeneracy of optimization-based ICP algorithms has been extensively studied. The pioneering work by Zhang *et al.* [25] analytically related the minimal eigenvalue of the Hessian of the optimization to the degeneracy factor and introduced a solution-remapping strategy that updates only the well-conditioned components of the state to handle degenerate cases. Building on this, Hinduja *et al.* [75] employed a Hessian condition number to define an eigenvalue threshold and proposed a degeneracy-aware partial factor for loop-closure in underwater SLAM. These SOTA methods have since been widely adopted in robotics, inspiring new extensions [76]–[78]. Daehan *et al.* [79] propose to leverage a hybrid point-to-point and point-to-plane error metric to address geometric degeneracy in ICP-based registration. Despite its effectiveness, this formulation may still lead to weakly constrained optimization directions in extremely degenerate environments where planar features dominate (see Figure 4).

To explicitly mitigate the lidar ICP degeneracy, Tuna *et al.* [80] introduce a fine-grained degeneracy detection and impose hard constraints along identified degenerate directions to stabilize the optimization under degeneracy. A follow-up study [26] provided a comprehensive investigation of



(a) Apollo 16 lunar mission. Courtesy NASA, assembly by Eric Jones [73].



(b) The Perseverance rover on Mars. Courtesy NASA/JPL-Caltech/MSSS [74].

Fig. 4: (a) Apollo 16 lunar surface imagery (NASA) and (b) Mars 2020 mission imagery (NASA/JPL-Caltech/MSSS) illustrating large-scale, sparsely structured terrain dominated by planar surfaces and gradual elevation changes. In such environments, strong geometric features cannot be assumed, making degeneracy-resilient navigation essential for reliable long-term planetary exploration.

degeneracy-resilient techniques for lidar localization, and showed that soft-constrained optimization can yield improved performance in complex, poorly conditioned environments when combined with carefully tuned heuristics. To account for the scale difference between translation and rotation elements, the degeneracy detection in [80] and [26] analyze translational and rotational Hessian blocks separately and ignore their mutual correlation. However, this separation may lead to inconsistent degeneracy detection in coupled motion scenarios, such as motion relative to a tilted planar surface, where translation and rotation are jointly constrained by the observed geometry.

In this paper, we present a FMCW LT&R system designed to achieve reliable autonomous navigation even in geometrically degraded environments. We first extend a Doppler velocity-based correspondence-free lidar-inertial odometry to include pose uncertainty estimation, enabling uncertainty propagation from odometry into the localization process. To improve scan-to-map localization robustness and efficiency, we leverage Gaussian curvature information extracted from the lidar point cloud. During the teach phase, per-point curvature is computed and stored in local submaps, and subsequently exploited in the repeat phase to enable curvature-aware down-sampling and data association. For scan-to-map ICP localization, we introduce a block-scaling formulation that normalizes rotational and translational components for consistent degeneracy detection, followed by a solution-remapping scheme similar to Hinduja *et al.* [75] to mitigate ill-conditioned updates.

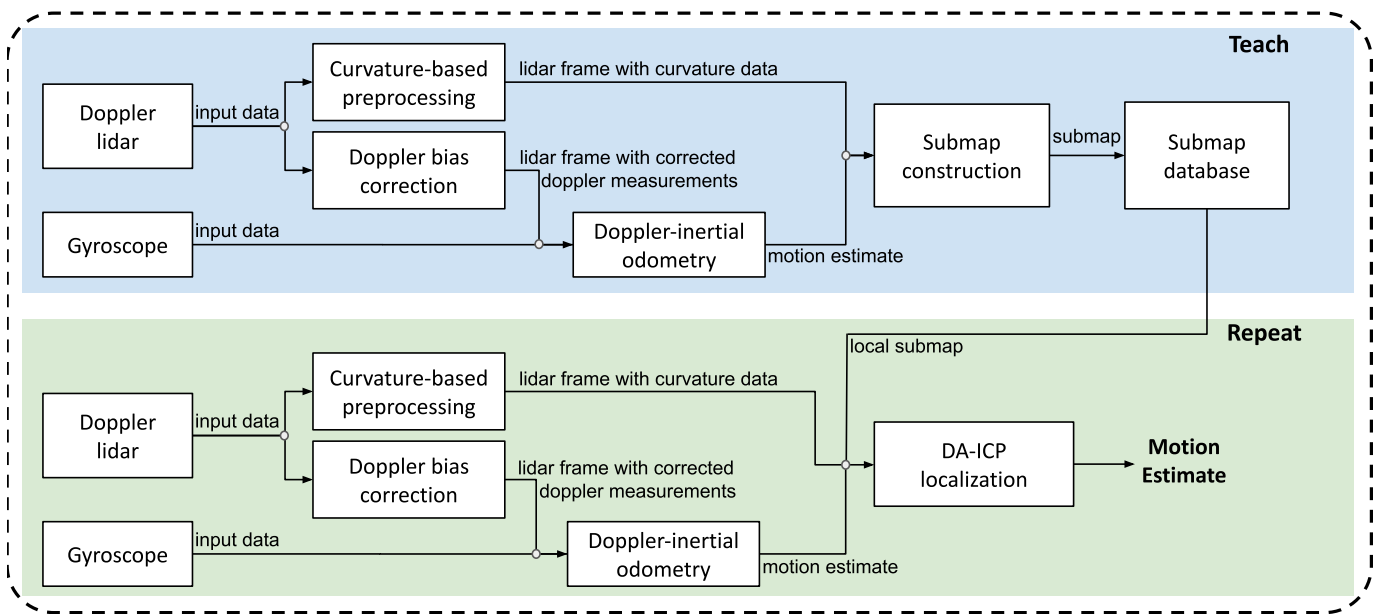


Fig. 5: An overview of the proposed Doppler LT&R system, showing the interaction between modules in the teach and repeat passes. During the teach pass, Doppler velocity and gyroscope measurements are used to estimate correspondence-free Doppler-inertial odometry, referred to throughout as Doppler odometry, while curvature information is computed and stored in local submaps. During the repeat pass, incoming lidar scans are processed using the same curvature-based preprocessing and combined with Doppler odometry to provide a motion prior. Scan-to-map localization is performed using degeneracy-aware ICP (DA-ICP) optimization against the stored submaps to refine the robot pose and enable closed-loop path following in geometrically challenging environments.

To the best of our knowledge, this is the first FMCW LT&R system capable of achieving reliable closed-loop navigation across a wide range of real-world outdoor environments, from highly structured feature-rich areas to severely degenerated feature-less scenarios.

III. METHODOLOGY

A. Problem Formulation

We propose a novel Doppler LT&R navigation framework that maintains robustness in environments with limited geometric features. The structure of the T&R pose graph is illustrated in Figure 2, and the overall architecture of our proposed system is illustrated in Figure 5. We use the following notation:

- k denotes the current robot frame being estimated,
- v denotes the vertex frame from odometry,
- m denotes the submap frame associated with vertex v from the teach pass,
- s denotes the lidar sensor frame,
- $\mathbf{T}_{m,s}$ denotes the transformation that aligns the live lidar point cloud scan in the sensor frame, \mathcal{F}_s , to the submap frame, \mathcal{F}_m ,
- $\hat{\mathbf{T}}_{k,k-1}$ denotes the latest odometry estimate from the previous frame, \mathcal{F}_{k-1} , to the current frame, \mathcal{F}_k ,
- $\hat{\mathbf{T}}_{k,v}$ denotes the pose estimate from the vertex frame, \mathcal{F}_v , to the current robot frame, \mathcal{F}_k .

The goal is to achieve reliable autonomous navigation in geometrically degenerate environments containing sparse features. In both the teach and repeat passes, we use the correspondence-free Doppler-inertial odometry [23], referred to as Doppler odometry, to estimate the frame-to-frame motion $\hat{\mathbf{T}}_{k,k-1}$ by leveraging the per-point radial velocity and

gyroscope measurements from the FMCW lidar. To perform localization, we introduce a curvature-augmented, degeneracy-aware ICP (DA-ICP) algorithm that aligns the live lidar scan to the submap and, together with the Doppler odometry prior, provides a robust estimate of $\hat{\mathbf{T}}_{k,v}$. This combination of Doppler odometry and robust DA-ICP localization enables consistent pose estimation and autonomous path following even in geometrically challenging environments where traditional lidar-based methods fail.

B. Curvature-Based Preprocessing

A common lidar preprocessing pipeline, such as the method described by Burnett *et al.* [41], typically relies on voxel-grid downsampling followed by principal component analysis (PCA)-based plane feature extraction. While effective in structured environments, this approach has limitations in degenerate environments. Uniform voxel downsampling treats all points equally and therefore tends to preserve large planar regions, such as the ground plane, while discarding small, but informative, geometric features. As a result, the downsampled cloud can fail to retain the geometrically distinctive features that support reliable data association, particularly in environments dominated by planar surfaces.

To address this, our preprocessing pipeline adopts a curvature-based downsampling method most similar to the method by [50]. Rather than uniformly subsampling the cloud, we first compute a per-point curvature estimate that captures local surface variation. For each point, a k -nearest neighbour search is performed using a KD-tree, and PCA is applied to obtain an initial estimate of the surface normal and principal directions. Since PCA yields surface normals up to a

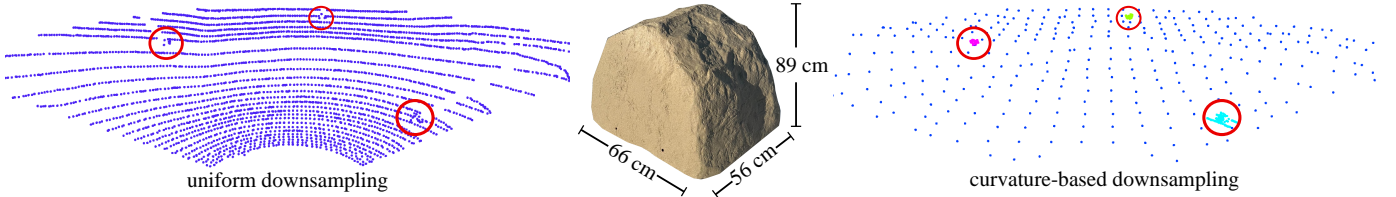


Fig. 6: Uniform downsampling (left) removes points indiscriminately across the scene, while curvature-based downsampling (right) preserves geometric features with high curvature, such as the rocks, and reduces redundant planar points. The curvature-based downsampled frame is coloured by curvature cluster.

sign ambiguity, the normal orientation is disambiguated by enforcing consistency with the lidar viewpoint, ensuring that normals face the sensor origin. The point neighbourhood is then expressed in a local tangent frame and fitted with a quadratic surface of the form

$$z(u, v) = ax^2 + bxy + cy^2 + dx + ey + f. \quad (1)$$

The coefficients of this fit yield the first and second fundamental forms, from which curvature, κ , is computed as

$$\kappa = \frac{ln - m^2}{eg - f^2}, \quad (2)$$

where (l, m, n) and (e, f, g) denote the components of the second and first fundamental forms, respectively. This quadratic fit refines the curvature estimate beyond what PCA alone can compute, enabling the detection of smaller geometric differences such as ridges, or transitions between different surface patches (e.g., asphalt versus grass).

The point cloud is then clustered into regions that share a similar curvature value. First, points with curvature below a threshold are classified as approximately planar and are grouped into a single cluster. Non-planar points are then clustered via a union-find region-growing procedure: each point searches for nearby neighbours within a fixed radius, and clusters are formed by merging connected sets of non-flat points. Small clusters, typically from noise or outliers, are removed based on a minimum cluster size criterion.

This clustering enables selective, geometry-aware downsampling. Each cluster is processed independently, and its mean curvature determines the voxel size used. Low-curvature clusters (e.g., ground plane, building facades) are aggressively downsampled using a larger voxel size, reducing redundant data in areas with low information. High-curvature clusters, which contain the most informative points for scan registration, are downsampled at a smaller resolution to preserve detail even when these features are sparse. An example of curvature-based point cloud downsampling, using a scene containing three artificial rocks placed on a flat airport runway, is illustrated in Figure 6. The resulting point cloud retains a dense sampling of the geometrically rich regions, while significantly reducing redundant planar points.

C. Doppler Odometry

As we target navigating in environments with non-distinctive or repetitive geometric environments, we adopt the Doppler odometry method presented by Yoon *et al.* [23],

a geometry-independent and correspondence-free odometry estimator. We provide a brief summary and refer the reader to [23] for more detail.

The state of the Doppler odometry only contains the 6-DOF vehicle body velocities $\varpi(t)$, where ϖ is a 6×1 vector containing the body-centric linear and angular velocities. The continuous-time estimation framework of Barfoot *et al.* [81] is applied to estimate the trajectory as a Gaussian process (GP), which allows each measurement to be applied at their exact measurement times. The relative pose estimate is computed via numerical integration.

The vehicle velocity prior is modelled as White-Noise-on-Acceleration (WNOA)

$$\dot{\varpi}(t) = \mathbf{w}(t), \quad \mathbf{w}(t) \sim \mathcal{GP}(\mathbf{0}, \mathbf{Q}_c \delta(t - t')), \quad (3)$$

where \mathbf{Q}_c is the power spectral density matrix. Incorporating the vehicle kinematics by penalizing velocities in the lateral, vertical, roll, and pitch dimensions, the kinematic residual term is

$$\mathbf{e}_{\text{kin},k} = \mathbf{H} \varpi_k, \quad (4)$$

where a constant \mathbf{H}_{kin} extracts the dimensions of interest.

The residual model for Doppler measurements is

$$e_{\text{dop},i} = y_{\text{dop},i} - \frac{1}{\|\mathbf{q}_i\|} [\mathbf{q}_i^\top \ \mathbf{0}] \mathcal{T}_{s,r} \varpi(t_i) - h(\psi_i), \quad (5)$$

where $y_{\text{dop},i}$ is the i th Doppler measurement, $\mathbf{q}_i \in \mathbb{R}^3$ are the corresponding point coordinates in the sensor frame, and $\mathcal{T}_{s,r} = \text{Ad}(\mathbf{T}_{s,r})$ is the known extrinsic adjoint transformation between the sensor and robot. This error measures the discrepancy observed between the measured radial velocity and the predicted radial velocity induced by the vehicle's motion. Due to the continuous-time formulation, the body-centric velocity can be conveniently queried using linear interpolation [81] as

$$\varpi(\tau) = (1 - \alpha) \varpi_{k-1} + \alpha \varpi_k, \quad \alpha = \frac{\tau - t_{k-1}}{t_k - t_{k-1}}, \quad (6)$$

with $\tau \in [t_{k-1}, t_k]$. Therefore, $\varpi(t_i) \in \mathbb{R}^6$ is the vehicle velocity queried at the lidar sensor measurement time t_i , and $h(\psi_i)$ is the Doppler velocity bias calibrated offline using the linear regression model from [23].

As the angular velocity is unobservable with Doppler measurements from one FMCW sensor [23], gyroscope data is used to estimate the angular velocity. The residual model is

$$\mathbf{e}_{\text{gyro},j} = \mathbf{y}_{\text{gyro},j} - \mathbf{R}_{s,r} \mathbf{D} \varpi(t_j) - \mathbf{b}_{\text{gyro}}, \quad (7)$$

where $\mathbf{y}_{\text{gyro},j} \in \mathbb{R}^3$ is the j th angular velocity measurement in the sensor frame, and $\mathbf{R}_{s,r} \in SO(3)$ is the known extrinsic rotation between the sensor and robot. The constant 3×6 projection matrix \mathbf{D} removes the translational elements of body-centric velocity $\boldsymbol{\omega}(t_j)$ queried at timestamp t_j . Since the gyroscope bias \mathbf{b}_{gyro} is reasonably constant in practice, we compute the value of \mathbf{b}_{gyro} by averaging the gyroscope's angular velocity measurements over 30 seconds while the robot is stationary. During the repeat pass, the gyroscope bias is updated using the method described in Appendix A.

With the motion prior and the Doppler and gyroscope measurements, the odometry is formulated as linear continuous-time batch estimation using a Maximum A Posteriori (MAP) problem

$$J_{\text{odom}} = \sum_k (\phi_{\text{wnoa},k} + \phi_{\text{kin},k}) + \sum_i \phi_{\text{dop},i} + \sum_j \phi_{\text{gyro},j}, \quad (8)$$

where the WNOA motion prior factor $\phi_{\text{wnoa},k}$, vehicle kinematic factor $\phi_{\text{kin},k}$, Doppler measurement factor $\phi_{\text{dop},i}$, and gyroscope measurement factor $\phi_{\text{gyro},j}$ are

$$\begin{aligned} \phi_{\text{wnoa},k} &= \frac{1}{2} (\boldsymbol{\omega}_k - \boldsymbol{\omega}_{k-1})^\top \mathbf{Q}_k^{-1} (\boldsymbol{\omega}_k - \boldsymbol{\omega}_{k-1}), \\ \phi_{\text{kin},k} &= \frac{1}{2} \mathbf{e}_{\text{kin},k}^\top \mathbf{Q}_z \mathbf{e}_{\text{kin},k}, \\ \phi_{\text{dop},i} &= \frac{1}{2} (e_{\text{dop},i})^2 R_{\text{dop}}^{-1}, \\ \phi_{\text{gyro},j} &= \frac{1}{2} \mathbf{e}_{\text{gyro},j}^\top \mathbf{R}_{\text{gyro}}^{-1} \mathbf{e}_{\text{gyro},j}. \end{aligned} \quad (9)$$

We solve the joint optimization problem and incrementally marginalize out the past velocity states to compute the latest velocity $\boldsymbol{\omega}_k$ (e.g., a filter implementation that handles measurements asynchronously). The relative pose estimate is approximated by numerically integrating:

$$\hat{\mathbf{T}}_{k,k-1} \approx \prod_{i=1}^S \exp(\Delta t \boldsymbol{\omega}(t_{k-1} + i\Delta t)^\wedge), \quad (10)$$

where S is the number of interpolation steps, $\exp(\cdot)$ is the exponential map, and $(\cdot)^\wedge$ transforms an element of \mathbb{R}^6 into a member of Lie algebra $\mathfrak{se}(3)$ [82].

In addition to estimating the vehicle velocity and relative poses, we derived the associated pose uncertainty not presented in [23], which allows us to propagate the uncertainties from the Doppler odometry estimates into the localization step.

a) Covariance of Interpolated Velocities: The velocity covariance at the query time τ , denoted $\mathbf{P}(\boldsymbol{\omega}_\tau, \boldsymbol{\omega}_\tau)$, is obtained by combining the batch-estimated covariance between consecutive frame velocities with the integrated process noise. Specifically, from the batch estimation we have the joint covariance

$$\mathbf{P}(\boldsymbol{\omega}_{t_{k-1}}, \boldsymbol{\omega}_{t_k}) = \mathbf{A}_{\text{odom}}^{-1}, \quad (11)$$

where \mathbf{A}_{odom} is the Hessian matrix of the Doppler odometry least-squares problem, and the inverse arises naturally from solving the linear system $\mathbf{A}_{\text{odom}} \mathbf{x} = \mathbf{b}_{\text{odom}}$ with $\mathbf{x} = [\boldsymbol{\omega}_{t_{k-1}}^\top \boldsymbol{\omega}_{t_k}^\top]^\top$.

To query the covariance at an intermediate time $\tau \in [t_{k-1}, t_k]$, we interpolate using the Gaussian process framework. Following the continuous-time WNOA model, the mean

velocity is linearly interpolated with the interpolation factor from (6). The corresponding interpolated covariance is

$$\begin{aligned} \mathbf{P}(\boldsymbol{\omega}_\tau, \boldsymbol{\omega}_\tau) &= [(1-\alpha)\mathbf{1}_6 \quad \alpha\mathbf{1}_6] \mathbf{P}(\boldsymbol{\omega}_{t_{k-1}}, \boldsymbol{\omega}_{t_k}) \begin{bmatrix} (1-\alpha)\mathbf{1}_6 \\ \alpha\mathbf{1}_6 \end{bmatrix} \\ &+ (1-\alpha)(\tau - t_{k-1}) \mathbf{Q}_c. \end{aligned} \quad (12)$$

following [83].

The first term propagates the uncertainty from the batch-estimated velocities, while the second term accounts for the accumulated process noise between t_{k-1} and τ under the WNOA prior. This formulation ensures that both correlations between frame velocities and the continuous-time process noise are captured in the interpolated covariance.

b) Numerical Pose Integration with Uncertainty: To compute the relative pose between frames, we numerically integrate the interpolated body-centric velocities over small timesteps Δt using the incremental update, described in (10). We now derive how uncertainty in these queried velocities propagates through each integration step.

We represent the pose at the previous timestep using the standard perturbation model:

$$\hat{\mathbf{T}}_{k-1} = \exp(\boldsymbol{\epsilon}_{k-1}^\wedge) \mathbf{T}_{k-1}, \quad \boldsymbol{\epsilon}_{k-1} \sim \mathcal{N}(\mathbf{0}, \boldsymbol{\Sigma}_{k-1}). \quad (13)$$

To understand how these uncertainties combine, we consider one integration step to the pose estimation at time τ , where we propagate the uncertainty

$$\hat{\mathbf{T}}_\tau = \exp((\boldsymbol{\phi} + \delta\boldsymbol{\phi})^\wedge) \mathbf{T}_{k-1}. \quad (14)$$

We first isolate the effect of the velocity noise. Using the first-order left Jacobian perturbation identity

$$\exp((\boldsymbol{\phi} + \delta\boldsymbol{\phi})^\wedge) \approx \exp((\mathcal{J}_l(\boldsymbol{\phi}) \delta\boldsymbol{\phi})^\wedge) \exp(\boldsymbol{\phi}^\wedge), \quad (15)$$

we separate the nominal increment from its perturbation [82] by using the $SE(3)$ left Jacobian, $\mathcal{J}_l(\boldsymbol{\phi})$.

Next, we incorporate the uncertainty in the previous pose. Substituting $\hat{\mathbf{T}}_{k-1} = \exp(\boldsymbol{\epsilon}_{k-1}^\wedge) \mathbf{T}_{k-1}$ and we can transport the pose perturbation [82] by

$$\begin{aligned} \hat{\mathbf{T}}_\tau &\approx \exp((\mathcal{J}_l(\boldsymbol{\phi}) \delta\boldsymbol{\phi})^\wedge) \\ &\exp((\text{Ad}(\exp(\boldsymbol{\phi}^\wedge)) \boldsymbol{\epsilon}_{k-1})^\wedge) \exp(\boldsymbol{\phi}^\wedge) \mathbf{T}_{k-1}, \end{aligned} \quad (16)$$

where $\text{Ad}(\cdot)$ is the adjoint operator of a Lie group.

The product of the two perturbations is now expressed in the Lie algebra. Applying the first-order Baker-Campbell-Hausdorff (BCH) expansion, we have

$$\begin{aligned} \boldsymbol{\xi}_\tau &= \ln(\exp((\mathcal{J}_l(\boldsymbol{\phi}) \delta\boldsymbol{\phi})^\wedge) \exp((\text{Ad}(\exp(\boldsymbol{\phi}^\wedge)) \boldsymbol{\epsilon}_{k-1})^\wedge))^\vee \\ &\approx \mathcal{J}_l(\boldsymbol{\phi}) \delta\boldsymbol{\phi} + \text{Ad}(\exp(\boldsymbol{\phi}^\wedge)) \boldsymbol{\epsilon}_{k-1}, \end{aligned} \quad (17)$$

which expresses the stochastic increment, $\boldsymbol{\xi}_\tau$, as the sum of the propagated velocity uncertainty and the transported prior pose uncertainty.

The covariance of this incremental update is therefore

$$\begin{aligned}
\mathbf{P}(\hat{\mathbf{T}}_\tau) &= \text{Cov}(\boldsymbol{\xi}_\tau) \\
&= \mathcal{J}_l(\phi)\text{Cov}(\phi)\mathcal{J}_l(\phi)^\top + \\
&\quad \text{Ad}(\exp(\phi^\wedge))\text{Cov}(\epsilon_{k-1})\text{Ad}(\exp(\phi^\wedge))^\top \\
&= \Delta t^2 \mathcal{J}_l(\phi)\mathbf{P}(\boldsymbol{\varpi}_\tau, \boldsymbol{\varpi}_\tau)\mathcal{J}_l(\phi)^\top + \\
&\quad \text{Ad}(\exp(\phi^\wedge))\boldsymbol{\Sigma}_{k-1}\text{Ad}(\exp(\phi^\wedge))^\top.
\end{aligned} \tag{18}$$

This expression is applied recursively across all integration steps to yield the full pose uncertainty at time k .

c) Recursive Pose Covariance Update: By applying this update recursively for all integration steps within a frame, we compute the mean pose and associated covariance at the end of the lidar frame. This allows the Doppler odometry estimator to maintain a consistent estimate of both pose and uncertainty:

$$\hat{\mathbf{T}}_k = \hat{\mathbf{T}}_{k,k-1}\hat{\mathbf{T}}_{k-1}, \quad \boldsymbol{\Sigma}_k = \mathbf{P}(\hat{\mathbf{T}}_k). \tag{19}$$

D. Mapping

In the T&R framework, mapping is achieved by incrementally building a series of local submaps that represent the vehicle's environment. Using the odometry estimates, the system continuously monitors the vehicle's motion, estimating the transformation between the latest submap, \mathcal{F}_m , and the current live lidar scan, \mathcal{F}_k . When the relative motion exceeds a predefined translation or rotation threshold, a new submap vertex \mathcal{F}_{m+1} is added. The submap at each new vertex is built by accumulating point clouds from the last five frames.

The reference maps are constructed during the teach pass using the Doppler odometry described above. We compute and store the curvature information of each point in a lidar frame using the curvature preprocessing method presented in Section III-B; however, during the teach pass, we do not apply the feature-specific downsampling. Instead of separately downsampling low- and high-curvature features, we apply the small feature voxel size to the full point cloud (equivalent to the preprocessing method presented in [41]). This retains a high point density in the stored submaps while preserving the curvature attributes required for feature matching during the repeat pass.

E. Degeneracy-Aware ICP Localization

1) Data Association: During the repeat pass, localization is performed by registering incoming scans to the previously constructed reference submaps using a degeneracy-aware ICP (DA-ICP) algorithm. We perform scan-to-map registration using point-to-plane ICP. To improve robustness in geometrically degenerate environments, we augment the standard spatial nearest-neighbour to include curvature information in the point correspondence search. This ensures that points are paired not only based on Euclidean proximity but also on local surface structure, reducing incorrect associations on planar regions that otherwise have ambiguous nearest neighbours.

Let $\mathcal{P}^{\text{raw}} = \{\mathbf{p}_i^{\text{raw}}\}_{i=1}^{N_p}$ and $\mathcal{Q}^{\text{raw}} = \{\mathbf{q}_j^{\text{raw}}\}_{j=1}^{N_q}$ denote the raw lidar scan and submap point clouds. For each scan point

$\mathbf{p}^{\text{raw}} \in \mathcal{P}^{\text{raw}}$, we denote $\mathcal{K}(\mathbf{p}^{\text{raw}}) \subset \mathcal{Q}^{\text{raw}}$ as the set of its k -nearest map neighbours, with $k = 8$. In this work, we propose using a joint spatial-curvature score that combines Euclidean proximity and curvature similarity to evaluate candidate map points $\mathbf{q}^{\text{raw}} \in \mathcal{K}(\mathbf{p}^{\text{raw}})$ for point correspondence. The correspondence score is defined as

$$c(\mathbf{p}^{\text{raw}}, \mathbf{q}^{\text{raw}}) = \frac{|\kappa_p - \kappa_q|}{\eta_\kappa} + \beta \frac{\|\mathbf{p}^{\text{raw}} - \mathbf{q}^{\text{raw}}\|}{\eta_d}, \tag{20}$$

where κ_p and κ_q denote point curvature corresponding to points \mathbf{p}^{raw} and \mathbf{q}^{raw} , η_κ and η_d are normalization scales that convert curvature (units m^{-1}) and Euclidean distance (units m) into comparable dimensionless quantities, and a weighting parameter β balances the influence of geometric similarity and spatial proximity. The optimal correspondence is selected as the candidate that minimizes this score over the neighbour set.

Rather than assuming fixed normalization constants, the scaling terms are estimated online using pseudo-random sampling of up to 1000 map points. Let $\mathcal{S}_Q \in \mathcal{Q}^{\text{raw}}$ be the sampled subset of map points, the spatial normalization scale is computed as the median nearest-neighbour distance among sampled map points, while the curvature normalization scale is computed as the median magnitude of the sampled curvature values

$$\begin{aligned}
\eta_d &= \text{median} \left(\min_{\mathbf{q} \in \mathcal{S}_Q} \left(\min_{\mathbf{q}' \in \mathcal{K}(\mathbf{q})} \|\mathbf{q} - \mathbf{q}'\| \right) \right), \\
\eta_\kappa &= \text{median} (|\kappa_q|).
\end{aligned} \tag{21}$$

This adaptive normalization finds the typical distance between map points and the typical submap curvature value to ensure stable correspondence selection across scenes with varying point densities and surface characteristics.

The use of a joint spatial-curvature correspondence score mitigates two key limitations of purely distance-based matching. In geometrically degenerate regions, such as large planar or weakly structured areas, multiple candidate map points often lie at similar Euclidean distances from a query point, leading to ambiguous or unstable correspondences when spatial proximity alone is used. Curvature information captures local surface geometry and helps distinguish structurally informative features, such as edges and corners, from less informative planar regions. However, relying solely on curvature may produce geometrically inconsistent matches. By jointly considering spatial proximity and geometric similarity, the proposed correspondence score yields more reliable and stable data association across diverse environments. The normalization step further prevents high-density or low-information regions from dominating the correspondence search, improving robustness across scenes with varying point densities and surface characteristics.

After selecting the best candidate match for each scan point, correspondences are further filtered using geometric consistency checks to remove unreliable matches. First, a spatial gating step discards pairs whose Euclidean separation exceeds a predefined threshold, ensuring that only locally consistent associations are retained. Once a reasonable initial alignment has been established, an additional filtering step removes correspondences with large point-to-plane residuals relative to

the target surface normal, rejecting associations that violate local planar geometry. These filtering steps improve robustness by eliminating outliers before the subsequent optimization stage.

2) *Degeneracy-Aware Optimization*: After curvature-based data association and correspondence filtering, we obtain the live lidar point cloud, $\mathcal{P} = \{\mathbf{p}_i\}$, and the corresponding local map points with normals $\mathcal{Q} = \{\mathbf{q}_i, \mathbf{n}_i\}$, where $\mathbf{n}_i \in \mathbb{R}^3$, $\|\mathbf{n}_i\| = 1$, estimated during the mapping process. The point-to-plane residual for each correspondence is modelled as

$$r_i(\mathbf{T}_{m,s}) = \mathbf{n}_i^\top \mathbf{D}(\mathbf{T}_{m,s} \mathbf{p}_i - \mathbf{q}_i), \quad (22)$$

where $\mathbf{T}_{m,s} = \{\mathbf{R}_{m,s}, \mathbf{t}_m^{s,m}\} \in SE(3)$ denotes the transformation from the lidar sensor frame to the local submap frame, and \mathbf{D} is a constant projection that removes the homogeneous element.

To account for measurement uncertainty in the point-to-plane formulation, we adopt a modelling approach similar to that in [84] and consider three independent noise sources. The first is the lidar range-bearing noise on each live lidar frame point \mathbf{p}_i , the second is the map-construction noise on the map point \mathbf{q}_i , and the third is the normal-estimation uncertainty on the normals \mathbf{n}_i . The lidar point covariance, $\Sigma_{p_i}^L$, obtained from a range-bearing noise model, is transformed into the map frame as $\Sigma_{p_i} = \mathbf{R}_{m,s} \Sigma_{p_i}^L \mathbf{R}_{m,s}^\top$. We assume an isotropic map-point covariance, $\Sigma_{q_i} = \sigma_m^2 \mathbf{1}_3$, and model normal uncertainty in the tangent plane as $\Sigma_{n_i} = \sigma_n^2 (\mathbf{1}_3 - \mathbf{n}_i \mathbf{n}_i^\top)$. With the three Jacobians,

$$\mathbf{J}_{p_i} = \mathbf{n}_i^\top \mathbf{R}_{m,s}, \quad \mathbf{J}_{q_i} = -\mathbf{n}_i^\top, \quad \mathbf{J}_{n_i} = (\mathbf{D}(\mathbf{T}_{m,s} \mathbf{p}_i - \mathbf{q}_i))^\top, \quad (23)$$

the scalar residual variance becomes

$$\sigma_{r_i}^2 = \mathbf{J}_{p_i} \Sigma_{p_i} \mathbf{J}_{p_i}^\top + \mathbf{J}_{q_i} \Sigma_{q_i} \mathbf{J}_{q_i}^\top + \mathbf{J}_{n_i} \Sigma_{n_i} \mathbf{J}_{n_i}^\top. \quad (24)$$

To formulate the weighted point-to-plane ICP objective function, we stack the residual vector

$$\mathbf{r}(\mathbf{T}_{m,s}) = \begin{bmatrix} r_1(\mathbf{T}_{m,s}) \\ \vdots \\ r_N(\mathbf{T}_{m,s}) \end{bmatrix} \in \mathbb{R}^N, \quad (25)$$

and the diagonal information matrix

$$\mathcal{I} = \text{diag} \left(\frac{1}{\sigma_{r_1}^2}, \dots, \frac{1}{\sigma_{r_N}^2} \right). \quad (26)$$

This yields the weighted point-to-plane ICP optimization as

$$\mathbf{T}_{m,s}^* = \arg \min_{\mathbf{T}_{m,s}} \mathbf{r}(\mathbf{T}_{m,s})^\top \mathcal{I} \mathbf{r}(\mathbf{T}_{m,s}). \quad (27)$$

We perturb the pose with a Lie algebra perturbation $\xi = [\mathbf{t}^\top \quad \boldsymbol{\theta}^\top]^\top \in \mathbb{R}^6$ with \mathbf{t} indicating the translational elements and $\boldsymbol{\theta}$ the rotational elements, and solve the optimization problem in (27) through a Gauss-Newton optimizer. The perturbation ξ is applied to an initial guess transformation $\bar{\mathbf{T}}_{m,s}$ as

$$\mathbf{T}_{m,s} = \exp(\xi^\wedge) \bar{\mathbf{T}}_{m,s}. \quad (28)$$

Linearizing the residual in (25) and setting the gradient to zero yields the Gauss-Newton normal equation:

$$\mathbf{H} \xi^* = \mathbf{b}, \quad (29)$$

where the Hessian matrix \mathbf{H} and right-hand-side vector \mathbf{b} are defined as

$$\mathbf{H} = \mathbf{J}^\top \mathcal{I} \mathbf{J}, \quad \mathbf{b} = -\mathbf{J}^\top \mathcal{I} \mathbf{r}, \quad (30)$$

and where \mathbf{J} is the Jacobian of the residual vector. Readers are referred to [15] for more details and derivations about point-to-plane ICP optimization.

The general principle of optimization degeneracy detection relies on checking the eigenvalues of the Hessian matrix [25], [75]; however, in point-to-plane ICP, the rotational and translational components operate on different numerical scales. Directly applying eigenvalue-based tests to the original Hessian matrix often leads to unreliable detection of any truly under-constrained directions [80]. To resolve this issue, we propose a block-scaled formulation that normalizes the rotational and translational elements of the Hessian matrix, enabling a more reliable assessment of geometric degeneracy.

To evaluate the relative conditioning of the rotational and translational components, we first marginalize each subspace using the Schur complement. With the partitioned Hessian matrix

$$\mathbf{H} = \begin{bmatrix} \mathbf{H}_{tt} & \mathbf{H}_{t\theta} \\ \mathbf{H}_{\theta t} & \mathbf{H}_{\theta\theta} \end{bmatrix}, \quad (31)$$

applying the Schur complement marginalization yields the marginalized rotational and translational information matrices,

$$\begin{aligned} \mathbf{H}_t^{\text{marg}} &= \mathbf{H}_{tt} - \mathbf{H}_{t\theta} \mathbf{H}_{\theta\theta}^{-1} \mathbf{H}_{\theta t} \\ \mathbf{H}_\theta^{\text{marg}} &= \mathbf{H}_{\theta\theta} - \mathbf{H}_{\theta t} \mathbf{H}_{tt}^{-1} \mathbf{H}_{t\theta}, \end{aligned} \quad (32)$$

each of which captures the information available in its respective subspace while marginalizing out the other. To unify the scale of rotational and translational elements, we define a scaling factor, ℓ , as the ratio of the dominant eigenvalues of $\mathbf{H}_\theta^{\text{marg}}$ and $\mathbf{H}_t^{\text{marg}}$,

$$\ell = \sqrt{\frac{\lambda_{\max}(\mathbf{H}_\theta^{\text{marg}})}{\lambda_{\max}(\mathbf{H}_t^{\text{marg}})}}. \quad (33)$$

Since we design the system for degenerate scenarios, we use the maximal eigenvalues instead of the sum of the eigenvalues to obtain a more stable unit scaling performance. Since real-world scenarios rarely contain directions that are fully degenerate for either rotation or translation, the proposed scaling factor remains well-behaved. The resulting ℓ factor normalizes the effective information across the two subspaces and directly informs the block-scaling matrix, \mathbf{S} , enabling consistent degeneracy detection and better-conditioned optimization.

Using our scaling factor, ℓ , we introduce a block-diagonal scaling matrix

$$\mathbf{S} = \begin{bmatrix} \mathbf{1}_3 & \mathbf{0} \\ \mathbf{0} & \ell \mathbf{1}_3 \end{bmatrix}, \quad (34)$$

and apply it to obtain the scaled perturbation $\tilde{\xi} = \mathbf{S} \xi$. Substituting this change of variables into the Gauss-Newton normal equation (29) yields the scaled system

$$\tilde{\mathbf{H}} \tilde{\xi} = \tilde{\mathbf{b}}, \quad (35)$$

with $\tilde{\mathbf{H}} = \mathbf{S}^{-T} \mathbf{H} \mathbf{S}^{-1}$ and $\tilde{\mathbf{b}} = \mathbf{S}^{-T} \mathbf{b}$. After solving for the optimal scaled perturbation, $\tilde{\xi}^*$, we map it back to the original incremental perturbation ξ^* :

$$\xi = \mathbf{S}^{-1} \tilde{\xi}^*. \quad (36)$$

Notably, the two procedures are algebraically identical. The block-scaling mechanism is a change of variables, it does not alter the solution of point-to-plane ICP optimization, but provides a unit-consistent coordinate system in which eigenvalue analysis and degeneracy detection can be performed reliably.

With the scaled and normalized Hessian matrix $\tilde{\mathbf{H}}$, we then apply the eigen-decomposition

$$\tilde{\mathbf{H}} = \mathbf{V}\mathbf{\Lambda}\mathbf{V}^\top, \quad (37)$$

where $\mathbf{V} = [\mathbf{v}_1 \ \cdots \ \mathbf{v}_6]$ contains the eigenvectors, and $\mathbf{\Lambda} = \text{diag}(\lambda_1, \dots, \lambda_6)$ stores the corresponding eigenvalues in descending order. We follow the same setup as [25], [75] and construct the matrices

$$\begin{aligned} \mathbf{V}_c &= [\mathbf{v}_1 \ \cdots \ \mathbf{v}_m] \\ \mathbf{V}_d &= [\mathbf{v}_{m+1} \ \cdots \ \mathbf{v}_6] \\ \mathbf{V}_{wc} &= [\mathbf{V}_c \ \mathbf{0} \ \cdots \ \mathbf{0}], \end{aligned} \quad (38)$$

where \mathbf{V}_c contains the well-conditioned eigenvector with $\lambda_i > \lambda_{\text{thresh}}$, \mathbf{V}_d stores the degenerated eigenvectors with $\lambda_i \leq \lambda_{\text{thresh}}$, and \mathbf{V}_{wc} contains the well-conditioned eigenvectors while zeroing out the degenerate directions. We determine the degenerate eigenvalues by checking the relative eigenvalue ratio. Specifically, an eigenvalue λ_i is considered as degenerate if its ratio to the largest eigenvalue, λ_{max} , exceeds a predefined eigen-ratio, γ ,

$$\frac{\lambda_{\text{max}}}{\lambda_i} \geq \gamma. \quad (39)$$

The corresponding eigenvalue threshold is computed by

$$\lambda_{\text{thresh}} = \frac{\lambda_{\text{max}}}{\gamma}. \quad (40)$$

In our system configuration, the predefined eigen-ratio is set to be $\gamma = 80$ for degeneracy detection.

With the degeneracy detection, we apply the same solution-remapping as illustrated in [75] and only update the well-conditioned directions,

$$\boldsymbol{\xi}_c^* = \mathbf{V}^{-\top} \mathbf{V}_{wc}^\top \boldsymbol{\xi}^*. \quad (41)$$

We then unscale the computed perturbation and compute the updated pose as

$$\hat{\mathbf{T}}_{m,s} = \exp((\mathbf{S}^{-1} \boldsymbol{\xi}_c^*)^\wedge) \bar{\mathbf{T}}_{m,s}. \quad (42)$$

To compute the covariance associated with the DA-ICP update, we operate on the scaled Hessian $\tilde{\mathbf{H}}$ and the constructed eigenvector matrices, \mathbf{V}_c and \mathbf{V}_d . Since we only update the well-conditioned directions, we retain the well-conditioned eigenvalues, $\mathbf{\Lambda}_c = \text{diag}(\lambda_i, \dots, \lambda_m)$, and zero out the degenerate components, producing the remapped Hessian, $\tilde{\mathbf{H}}_{rm} = \mathbf{V} \text{diag}(\mathbf{\Lambda}_c, \mathbf{0}) \mathbf{V}^\top$. To avoid singularity, we add a small regularization $\epsilon \mathbf{1}_6$, yielding the regulated remapped Hessian as

$$\begin{aligned} \tilde{\mathbf{H}}_r &= \tilde{\mathbf{H}}_{rm} + \epsilon \mathbf{1}_6 \\ &\approx \mathbf{V}_c \mathbf{\Lambda}_c \mathbf{V}_c^\top + \mathbf{V}_d (\epsilon \mathbf{1}_6) \mathbf{V}_d^\top. \end{aligned} \quad (43)$$

As a result, the scaled covariance can be calculated via pseudo-inverse of the regulated remapped Hessian:

$$\tilde{\mathbf{P}} = \tilde{\mathbf{H}}_r^{-1} = \mathbf{V}_c \mathbf{\Lambda}_c^{-1} \mathbf{V}_c^\top + \mathbf{V}_d (\epsilon \mathbf{1}_6)^{-1} \mathbf{V}_d^\top. \quad (44)$$

Finally, we unscale the covariance to map it back to the original perturbation space:

$$\hat{\mathbf{P}} = \mathbf{S}^{-1} \tilde{\mathbf{P}} \mathbf{S}. \quad (45)$$

After the DA-ICP alignment converges, we fuse its pose estimate with the motion prior from Doppler odometry to refine the pose estimate. We fuse the DA-ICP results with the prior information in a loosely coupled manner. The initial guess for the sensor-to-map transformation is

$$\mathbf{T}_{m,s}^{\text{init}} = (\mathbf{T}_{s,k} \check{\mathbf{T}}_{k,v} \mathbf{T}_{v,m})^{-1}, \quad (46)$$

where $\check{\mathbf{T}}_{k,v}$ is from odometry, $\mathbf{T}_{s,k}$ is the known robot-to-sensor extrinsic, and $\mathbf{T}_{v,m}$ is the transform from the reference submap to the current vertex.

To ensure a smooth and robust ICP correction, we wrap the ICP localization error in a robust cost function. We follow the square root formulation in [85] and define the ICP localization error as

$$\mathbf{e}_{\text{icp}} \triangleq \hat{\mathbf{P}}^{-\top/2} \ln \left(\hat{\mathbf{T}}_{m,s}^{-1} \mathbf{T}_{m,s}^{\text{init}} \right), \quad (47)$$

with $\hat{\mathbf{P}}^{-1/2}$ the matrix square root of $\hat{\mathbf{P}}$. The loosely coupled joint optimization problem is formulated as

$$\mathcal{J}_{\text{joint}} = \frac{1}{2} \mathbf{e}_{\text{prior}}^\top \mathbf{Q}_{\text{prior}}^{-1} \mathbf{e}_{\text{prior}} + \rho(\mathbf{e}_{\text{icp}}), \quad (48)$$

where $\mathbf{Q}_{\text{prior}}$ is the covariance matrix associated with the prior, $\rho(\cdot)$ indicates the robust cost function, and $\mathbf{e}_{\text{prior}}$ is computed as

$$\mathbf{e}_{\text{prior}} = \ln(\check{\mathbf{T}}_{k,m} \mathbf{T}_{k,m}^{-1})^\vee. \quad (49)$$

We use the Cauchy robust cost function with the hyperparameter $c = 0.1$ [86], and solve the joint optimization problem to obtain the posterior pose estimate $\hat{\mathbf{T}}_{k,v}$ via Gauss-Newton using the STEAM optimization library [87].

3) *Outlier Rejection*: To prevent unreliable localization updates from corrupting the final pose estimate, we perform a simple post-alignment consistency check between the fused DA-ICP pose, $\hat{\mathbf{T}}_{k,v}$, and the incoming odometry estimate, $\check{\mathbf{T}}_{k,v}$. We compute the relative transform

$$\mathbf{T}_{\text{diff}} = \hat{\mathbf{T}}_{k,v} \check{\mathbf{T}}_{k,v}^{-1}, \quad (50)$$

and map it to a 6D vector using the matrix logarithm. The translation and rotation components of this vector quantify how far the joint solution has moved from the odometry estimate.

If either component exceeds preset thresholds, the fused result is considered inconsistent, typically due to incorrect surface alignment or insufficient geometric structure, and the system falls back to using the odometry estimate.

IV. EXPERIMENTS

A. Experimental Setup and Field Test Environments

We perform all experiments using a Warthog unmanned ground vehicle (UGV) equipped with an Aeva Aeries II FMCW lidar sensor, set to use a 120° horizontal field of view, a 19.2° vertical field of view, and a 40 m range. The sensor operates at 10 Hz and is equipped with an IMU, from which we use gyroscope measurements.

We use three environments that differ in geometric structure to compare and evaluate the proposed pipeline in environments ranging from feature-less to feature-rich. Our pipeline is tested on 1.1 km of closed-loop driving, and we perform a comparative study using an additional 2.6 km of closed-loop tests. The routes used in our evaluation are:

- Space Agency (SA) Routes — Two routes collected in the Analogue Terrain at a SA with a range of geometric feature density. Segments of these routes are feature-rich with buildings, trees, and rocks, while other segments are feature-limited with rocks and terrain variation (hills/craters).
- Campus Route — A route with many clear geometric features including buildings, cars, trees, and a fence. This route provides the baseline against which we compare our pipeline to standard LT&R performance.
- Airport Route — A route collected on an airport runway. The runway is feature-less, therefore rocks are added to the scene to introduce sparse geometric structure.

We obtained the groundtruth measurements on the Campus Route and the Airport Route using a Leica Nova MS50 MultiStation, which continuously tracks a Leica GRZ4 360° prism mounted on a Warthog UGV, as seen in Figure 7. The Leica total station provides millimetre-level positional accuracy under clear line-of-sight conditions, making it well suited for our purpose of evaluating closed-loop performance in feature-less environments. For the SA Route, we planned to leverage a NovAtel RTK-GPS system as the groundtruth; however, the GPS data from the base station was unavailable during our field test, as explained in Appendix B, resulting in the absence of accurate groundtruth data for evaluation.

B. Evaluation Metrics

To quantify the performance of our proposed T&R system, we use two path-tracking error metrics: lateral root mean squared error (RMSE) computed using groundtruth measurements from a Leica total station, and T&R self-estimated lateral RMSE. Both metrics evaluate how accurately the vehicle follows the teach pass reference trajectory by measuring the errors that arise from both localization and vehicle control.

The lateral RMSE measures the perpendicular deviation of the repeat trajectory from the reference teach trajectory. Using the groundtruth measurements, we first identify the moving segment of each trajectory to exclude the stationary periods at the beginning and end. The teach and repeat trajectories are then aligned by the cumulative arclength along the path. At each point along the path, the vector difference between teach and repeat positions is projected onto the tangent of the reference path, and the component orthogonal to this tangent is the lateral error. The root mean square value of this error over the moving segment constitutes the lateral RMSE.

The self-reported error uses the internal estimate of the lateral error produced by the T&R pipeline. For each vertex along the repeat trajectory, we compute the signed lateral distance from the reference teach path using the stored pose graph representation, which encodes the relative positions of each vertex with respect to those in the teach trajectory. The

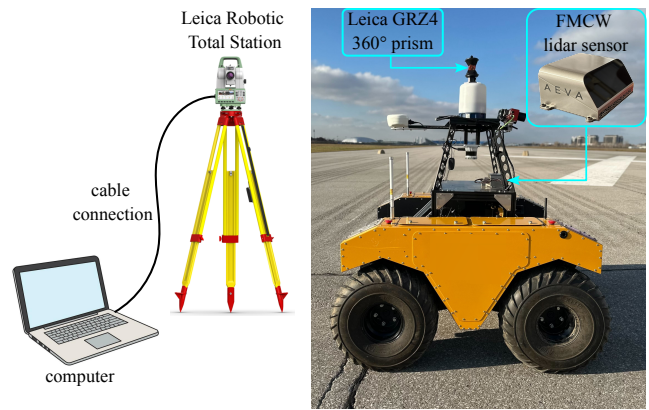


Fig. 7: Warthog unmanned ground vehicle (UGV) equipped with an Aeva Aeries II FMCW lidar sensor and a survey-grade prism. A Leica robotic total station tracks the prism to provide millimetre-level groundtruth position measurements for closed-loop navigation field experiments.

resulting self-reported lateral RMSE provides an estimate of the path-tracking error without the use of external groundtruth data. A small discrepancy between the measured lateral RMSE and the T&R-estimated RMSE indicates that the system’s internal uncertainty estimates are reliable, suggesting accurate localization.

C. Pipeline Performance

To evaluate the contributions of each component in our proposed T&R pipeline, we compare four variants:

- 1) Curvature-based preprocessing, Doppler Odometry, DA-ICP localization (ours),
- 2) Curvature-based preprocessing, Doppler Odometry, Default point-to-plane ICP localization,
- 3) Default preprocessing, Doppler Odometry, Default point-to-plane ICP localization,
- 4) Default preprocessing, Default ICP Odometry, Default point-to-plane ICP localization (default LT&R [41]).

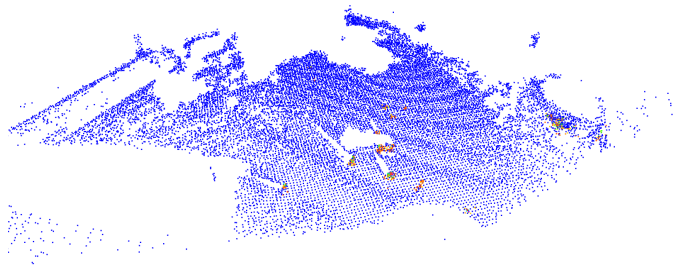
This comparison allows us to isolate the effect of each module and assess how each impacts overall path-tracking performance. For each route and pipeline variant, three repeat runs were performed, and the reported RMSE values correspond to the mean error across the trials to reduce the influence of run-to-run variability.

a) SA Routes: Figure 9 and Table I present the results for two SA routes. Only two pipelines are tested on these routes, our proposed system and default LT&R. Despite logging GPS data during these tests to use as groundtruth, we do not believe that the quality of the GPS signal without base-station corrections is sufficient to reliably represent the measured errors (see Figure 11 in Appendix B); therefore, we only present the internally computed error from our localization. We did not have the Leica total station setup in this environment.

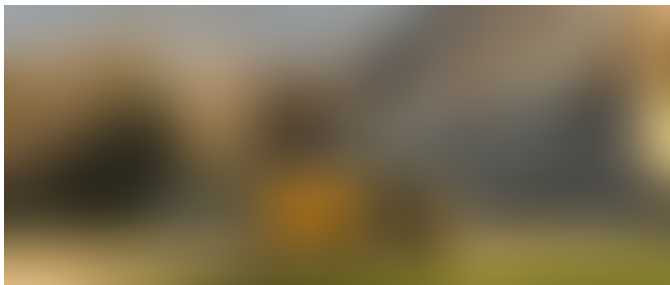
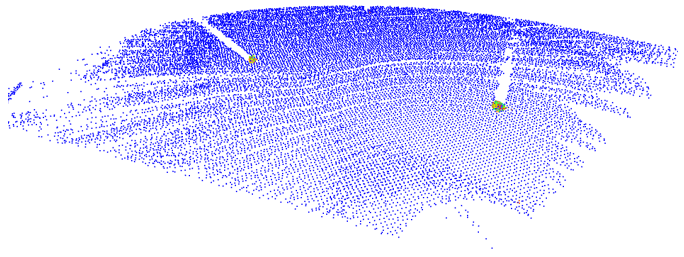
Across both SA routes, the proposed system achieves path-tracking accuracy comparable to that of the default LT&R pipeline. The SA environment, while less structured than the Campus route, still contains sufficient geometric structure for



(a) Space Agency (SA) Routes



(b) Airport Route



(c) Campus Route



Fig. 8: Experimental environments used for field evaluation. The left column shows representative images captured during the experiments, while the right column presents the corresponding lidar point clouds coloured by curvature, where blue indicates near-zero curvature and non-planar features appear in different colours. The experiments were conducted across environments with varying geometric structure, ranging from feature-rich (campus route), feature-limited (SA planetary analogue route), to feature-less (airport runway route). Image (c) is intentionally blurred for double-blind review.

the baseline pipeline to avoid divergence. Consequently, neither system exhibits catastrophic failure, and the self-reported errors remain comparable throughout the runs.

Notably, on SA route 2, the proposed pipeline achieves lower self-reported error compared to the default pipeline. This suggests that the robustness additions in our proposed pipeline prevent drift in regions where structure is weaker. Overall, these results indicate that the proposed method can preserve baseline accuracy in moderately structured environments, and remain stable in areas where geometric constraints are reduced.

b) Airport Route: Figure 10 and Table I show that the Airport route results vary the greatest across pipelines. This route is extremely feature-sparse, containing long stretches of asphalt, grass, and occasional rock features. Under these conditions, all pipelines using default ICP to localize fail to complete the route. In Variants 3 and 4, divergence occurs early in the run due to unreliable point correspondences. Variant 3 progresses further along the route compared to Variant 4 due to using the Doppler odometry method to create the reference maps. Variant 2, which uses the curvature-based

preprocessing and Doppler odometry, is able to complete half the route. This shows that the curvature-based preprocessing is successfully aiding in the quality of point correspondences, even in otherwise correspondence-poor environments.

Only our proposed pipeline successfully completes the entire route. The combination of curvature-based preprocessing and DA-ICP enables scan-to-map alignment even when geometric structure is weak. Doppler odometry provides a consistent, correspondence-free motion prior. DA-ICP then updates only the well-constrained directions of the estimate and relies on the odometry estimate in the poorly constrained directions. This allows the system to remain stable over large stretches where ICP alone cannot operate reliably, ultimately enabling successful closed-loop navigation in a challenging environment. Although our proposed system also leads to an approximate average of 40 cm closed-loop tracking error over three repeats, we argue that in such geometrically challenging environments, mission success should take precedence over precise trajectory tracking.

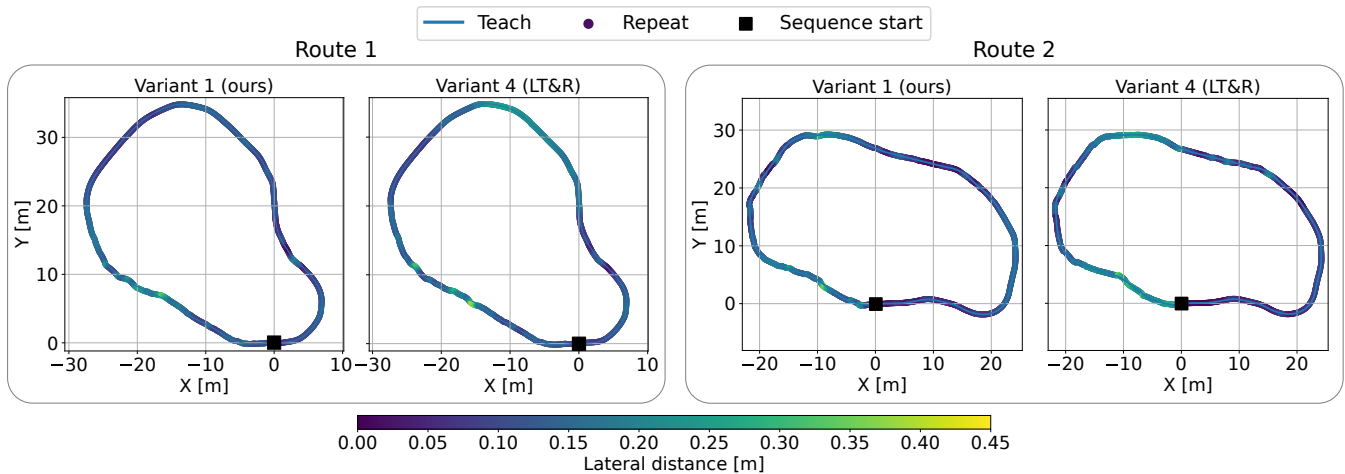


Fig. 9: Closed-loop navigation performance (top-down view), evaluated using self-reported path-tracking error, on two SA routes. For each route, the left plot presents the proposed degeneracy-resilient T&R system, and the right plot presents the Doppler LT&R baseline. In this moderately structured environment, both systems complete the routes with comparable path-tracking performance, showing that the proposed method maintains nominal performance in well-constrained scenarios.

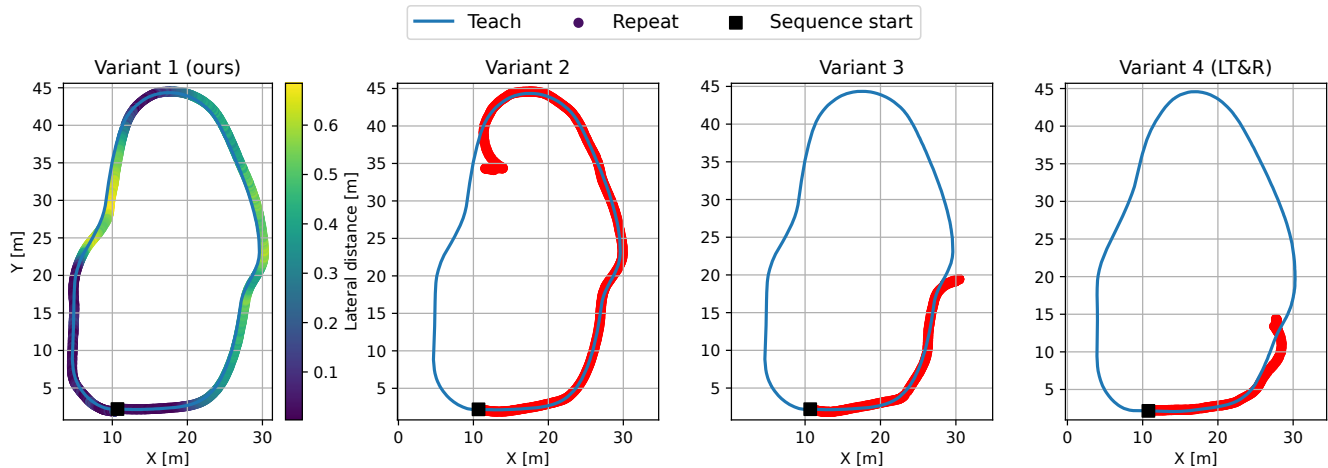


Fig. 10: Closed-loop navigation performance (top-down view) of four pipeline variants on a feature-limited airport runway, evaluated using millimetre-level groundtruth measurements from a Leica total station. Only the proposed pipeline successfully completes the entire route, while the remaining variants diverge due to unreliable scan-to-map alignment in the absence of sufficient geometric structure.

c) *Campus Route*: Table I shows that all four pipelines successfully complete the Campus route. The default LT&R pipeline achieves the lowest tracking error overall, which is expected due to the strong geometric structure of the environment and the effectiveness of ICP-based odometry and localization when reliable correspondences can be made.

Variants 2 and 3, both using Doppler odometry, produce similar lateral errors; however, Variant 2 shows a slight improvement over Variant 3, indicating that the curvature-based preprocessing provides a modest benefit. By incorporating curvature information into correspondence selection, Variant 2 improves the reliability of data association, particularly in locally planar or weakly structured areas where purely distance-based matching is ambiguous, resulting in more consistent ICP scan matching.

Although the proposed T&R pipeline obtains the highest lateral error among the four, its performance remains close to the Doppler-based baseline (Variant 2), with a difference

of only 3.5 cm. This marginal gap can be attributed to the use of a conservative degeneracy threshold, with an eigen-ratio of 80. The system is intentionally tuned for geometrically degenerate environments; therefore, a low threshold is adopted to update only directions that are strongly well-conditioned. In feature-rich environments, this conservative setting may restrict updates even when sufficient geometric constraints are available, leading to slightly higher error.

To verify this interpretation, we performed an additional experiment increasing the eigen-ratio threshold to 2000 in the same feature-rich scenario. As shown in Table I, this relaxing the degeneracy detection reduces the performance gap and yields results comparable to the Variant 3 pipeline. This indicates that the remaining error difference largely reflects a robustness-accuracy trade-off. Since our system is designed to perform reliably in degenerate environments, we prioritize navigation robustness while incurring only minimal accuracy loss under feature-rich conditions.

TABLE I: Quantitative performance evaluation of the four pipeline variants. Results are averaged over three repeat runs. Lateral path-tracking error is reported in meters with ‘measured’ errors referring to the Leica total station groundtruth-measured errors and ‘T&R’ errors referring to the self-reported T&R-estimated errors.

Route	Pipeline Variant	Measured Lateral RMSE [m]	T&R Lateral RMSE [m]	Measured Max Lateral Error [m]	T&R Max Lateral Error [m]
SA 1	1 (ours) / param. 80	No GPS	0.136	No GPS	0.421
	4 (LT&R)	No GPS	0.141	No GPS	0.470
SA 2	1 (ours) / param. 80	No GPS	0.133	No GPS	0.367
	4 (LT&R)	No GPS	0.170	No GPS	0.510
Airport	1 (ours) / param. 80	0.406	0.138	0.868	0.574
	2	—————	—————	Failed	—————
	3	—————	—————	Failed	—————
	4 (LT&R)	—————	—————	Failed	—————
Campus	1 (ours) / param. 80	0.157	0.115	0.642	0.339
	1 (ours) / param. 2000	0.091	0.084	0.267	0.215
	2	0.117	0.089	0.387	0.328
	3	0.124	0.091	0.425	0.321
	4 (LT&R)	0.079	0.066	0.216	0.195

V. CONCLUSION

This paper presents a degeneracy-resilient T&R navigation system using a FMCW lidar for geometrically challenging environments. We extended a correspondence-free Doppler-inertial odometry method with pose uncertainty estimation, enabling principled uncertainty propagation into localization. To improve scan-to-map alignment under geometric degeneracy, we proposed a curvature-enhanced data association and introduced a block-scaled, eigenvalue-based degeneracy-aware ICP formulation that enables consistent detection and mitigation of ill-conditioned optimization directions.

The proposed system was evaluated in closed-loop field experiments across environments ranging from feature-rich to severely feature-limited. In structured environments, the system achieved tracking performance comparable to the baseline Doppler LT&R pipeline, with slightly higher error under conservative degeneracy thresholds that can be reduced through parameter tuning. In contrast, in a flat airport runway scenario, where ICP-based LT&R and other pipeline variants failed, the proposed system maintained reliable autonomous navigation, demonstrating robustness under extreme geometric degeneracy. By combining geometry-independent Doppler odometry with curvature-enhanced, degeneracy-aware localization, the system remains stable by updating only well-constrained motion directions while relying on odometry in degenerate subspaces. This makes the approach well suited for long-range autonomous navigation in unstructured environments, such as planetary surfaces, where strong geometric features cannot be assumed. Future work will focus on extending field validation with improved groundtruth coverage and longer trajectories.

APPENDIX

A. Online Gyroscope Bias Correction

To reduce drift caused by slowly varying IMU biases, we estimate the gyroscope bias online by comparing the

rotational motion implied by DA-ICP against the angular velocity measured by the IMU. As before, let $\mathbf{T}_{k,v}(t)$ denote the pose estimate from DA-ICP at time t . Given two successive estimates, $\mathbf{T}_{k,v}(t)$ and $\mathbf{T}_{k,v}(t - \Delta t)$, the relative motion is obtained via the logarithmic map,

$$\phi = \log\left(\mathbf{T}_{k,v}(t) \mathbf{T}_{k,v}^{-1}(t - \Delta t)\right)^\vee \in \mathfrak{se}(3), \quad (51)$$

where $\phi = [\mathbf{v}^\top \ \boldsymbol{\omega}^\top]^\top$ contains both translational and rotational components. The rotational velocity implied by ICP is then

$$\hat{\boldsymbol{\omega}} = \frac{\boldsymbol{\omega}}{\Delta t}. \quad (52)$$

Over the same interval, we compute the mean angular velocity measured by the IMU,

$$\bar{\boldsymbol{\omega}}_{\text{imu}} = \frac{1}{N} \sum_{j=1}^N \boldsymbol{\omega}_{\text{imu},j}, \quad (53)$$

where the sum is taken over all N gyroscope samples within the lidar frame time window. The bias estimate is obtained from the discrepancy between the IMU and ICP rotational rates

$$\mathbf{b}_\omega^{\text{new}} = \bar{\boldsymbol{\omega}}_{\text{imu}} - \hat{\boldsymbol{\omega}}. \quad (54)$$

Bias updates are applied only when sufficient motion has occurred (i.e., Δt exceeds a configurable threshold) and when the computed update is consistent with the prior estimate to avoid transient ICP errors. When accepted, we update the bias using an exponential moving average,

$$\mathbf{b}_\omega \leftarrow (1 - \zeta) \mathbf{b}_\omega + \zeta \mathbf{b}_\omega^{\text{new}}, \quad (55)$$

where $\zeta = 0.2$ in our implementation.

This correction prevents long-term drift arising from slowly varying gyroscope bias while avoiding aggressive updates during low-motion intervals or during ICP misalignment.

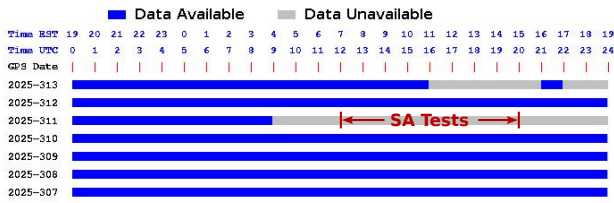


Fig. 11: Temporal availability of the nearest Global Navigation Satellite System (GNSS) station during the SA experiments. The grey shaded regions indicate periods when GNSS data was unavailable, demonstrating gaps in the groundtruth measurements used for performance evaluation. The red text indicates when the SA experiments were conducted.

B. GPS Availability during SA Tests

During the period when the SA experiments presented in this work were conducted, as indicated in Figure 11, data from the nearest GNSS station was unavailable. This unavailability was only discovered after the completion of the experimental testing. High-accuracy GPS positioning requires base station corrections and post-processing to reduce errors to the centimetre-level. Since the base station data was unavailable during our tests, the recorded GPS measurements were not sufficiently accurate to serve as groundtruth for evaluating closed-loop navigation performance. Consequently, measured errors could not be included in the performance analyses for the SA routes.

REFERENCES

- [1] J. Marshall, T. Barfoot, and J. Larsson, "Autonomous underground tramming for center-articulated vehicles," *Journal of Field Robotics*, vol. 25, no. 6-7, pp. 400–421, 2008.
- [2] K. Ebadi, L. Bernreiter, H. Biggie, G. Catt, Y. Chang, A. Chatterjee, C. E. Denniston, S.-P. Deschênes, K. Harlow, S. Khattak, *et al.*, "Present and future of SLAM in extreme environments: The DARPA SubT challenge," *IEEE Transactions on Robotics*, vol. 40, pp. 936–959, 2023.
- [3] T. Daoust, *Infrastructure-free mapping and localization for tunnel-based rail applications using 2D Lidar*. University of Toronto (Canada), 2017.
- [4] NASA, "Ingenuity Mars Helicopter," July 2020, <https://science.nasa.gov/mission/mars-2020-perseverance/ingenuity-mars-helicopter/>, last accessed on 2026-02-13.
- [5] A. Dzedzickis, J. Subačiūtė-Žemaitienė, E. Šutinys, U. Samukaitė-Bubnienė, and V. Bučinskas, "Advanced applications of industrial robotics: New trends and possibilities," *Applied Sciences*, vol. 12, no. 1, p. 135, 2021.
- [6] A. Krawciw, S. Lilge, L. Antonyshyn, and T. D. Barfoot, "Sharing the load: Distributed model-predictive control for precise multi-rover cargo transport," *arXiv preprint arXiv:2510.18766*, 2025.
- [7] P. Slowik and B. Sharpe, "Automation in the long haul: Challenges and opportunities of autonomous heavy duty trucking in the United States." ICCT Washington, DC, USA, 2018.
- [8] T. R. Gill, J. D. J. Gomez Jr, D. Pittman, M. Lewis, K. Beaton, S. Chappell, and P. Kessler, "Lunar surface cargo offloading concepts," in *51st International Conference on Environmental Systems (ICES 2022)*, no. ICES-2022-38, 2022.
- [9] P. Furgale and T. D. Barfoot, "Visual teach and repeat for long-range rover autonomy," *Journal of field robotics*, vol. 27, no. 5, pp. 534–560, 2010.
- [10] A. Krawciw and T. D. Barfoot, "Local maps are all you need: A review of topometric teach and repeat navigation," *Annual Review of Control, Robotics, and Autonomous Systems*, vol. 9, 2025.
- [11] D. Baril, S.-P. Deschênes, O. Gamache, M. Vaidis, D. LaRocque, J. Laconte, V. Kubelka, P. Giguère, and F. Pomerleau, "Kilometer-scale autonomous navigation in subarctic forests: challenges and lessons learned," *Field Robotics*, vol. 2, pp. 1628–1660, 2022.
- [12] P. Krüsi, P. Furgale, M. Bosse, and R. Siegwart, "Driving on point clouds: Motion planning, trajectory optimization, and terrain assessment in generic nonplanar environments," *Journal of Field Robotics*, vol. 34, no. 5, pp. 940–984, 2017.
- [13] A. Krawciw, N. Olmedo, F. Rehmatullah, M. Desjardins-Goulet, P. Toupin, and T. D. Barfoot, "Lunar rover cargo transport: Mission concept and field test," *IEEE Transactions on Field Robotics*, 2026.
- [14] P. J. Besl and N. D. McKay, "Method for registration of 3-D shapes," in *Sensor fusion IV: control paradigms and data structures*, vol. 1611. Spie, 1992, pp. 586–606.
- [15] F. Pomerleau, F. Colas, R. Siegwart, *et al.*, "A review of point cloud registration algorithms for mobile robotics," *Foundations and Trends® in Robotics*, vol. 4, no. 1, pp. 1–104, 2015.
- [16] C. D. Epp and T. B. Smith, "Autonomous precision landing and hazard detection and avoidance technology (ALHAT)," in *2007 IEEE aerospace conference*. IEEE, 2007, pp. 1–7.
- [17] F. Amzajerjian, D. Pierrottet, L. Petway, G. Hines, and V. Roback, "Lidar systems for precision navigation and safe landing on planetary bodies," vol. 8192. SPIE, 2011, pp. 27–33.
- [18] D. F. Pierrottet, F. Amzajerjian, L. Petway, B. Barnes, G. Lockard, and M. Rubio, "Linear FMCW laser radar for precision range and vector velocity measurements," *MRS Online Proceedings Library*, vol. 1076, no. 1, p. 10760406, 2008.
- [19] S. Royo and M. Ballesta-Garcia, "An overview of lidar imaging systems for autonomous vehicles," *Applied sciences*, vol. 9, no. 19, p. 4093, 2019.
- [20] F. Amzajerjian, L. Petway, G. Hines, B. Barnes, D. Pierrottet, and G. Lockard, "Doppler lidar sensor for precision landing on the Moon and Mars," in *2012 IEEE Aerospace Conference*. IEEE, 2012, pp. 1–7.
- [21] B. Hessel, H. Vhavle, and Y. Chen, "DICP: Doppler Iterative Closest Point Algorithm," in *Proceedings of Robotics: Science and Systems*, New York City, NY, USA, June 2022.
- [22] Y. Wu, D. J. Yoon, K. Burnett, S. Kammel, Y. Chen, H. Vhavle, and T. D. Barfoot, "Picking up speed: Continuous-time lidar-only odometry using doppler velocity measurements," *IEEE Robotics and Automation Letters*, vol. 8, no. 1, pp. 264–271, 2022.
- [23] D. J. Yoon, K. Burnett, J. Laconte, Y. Chen, H. Vhavle, S. Kammel, J. Reuther, and T. D. Barfoot, "Need for speed: Fast correspondence-free lidar-inertial odometry using doppler velocity," in *2023 IEEE/RSJ International Conference on Intelligent Robots and Systems (IROS)*. IEEE, 2023, pp. 5304–5310.
- [24] N. Gelfand, L. Ikemoto, S. Rusinkiewicz, and M. Levoy, "Geometrically stable sampling for the ICP algorithm," in *Fourth International Conference on 3-D Digital Imaging and Modeling, 2003. 3DIM 2003. Proceedings*. IEEE, 2003, pp. 260–267.
- [25] J. Zhang, M. Kaess, and S. Singh, "On degeneracy of optimization-based state estimation problems," in *2016 IEEE international conference on robotics and automation (ICRA)*. IEEE, 2016, pp. 809–816.
- [26] T. Tuna, J. Nubert, P. Pfreundschuh, C. Cadena, S. Khattak, and M. Hutter, "Informed, constrained, aligned: A field analysis on degeneracy-aware point cloud registration in the wild," *IEEE Transactions on Field Robotics*, 2025.
- [27] W. Churchill and P. Newman, "Experience-based navigation for long-term localisation," *The International Journal of Robotics Research*, vol. 32, no. 14, pp. 1645–1661, 2013.
- [28] M. Paton, K. MacTavish, L.-P. Berczi, S. K. van Es, and T. D. Barfoot, "I can see for miles and miles: An extended field test of visual teach and repeat 2.0," in *Field and Service Robotics: Results of the 11th International Conference*. Springer, 2017, pp. 415–431.
- [29] P. King, A. Vardy, and A. L. Forrest, "Teach-and-repeat path following for an autonomous underwater vehicle," *Journal of Field Robotics*, vol. 35, no. 5, pp. 748–763, 2018.
- [30] X. Qiao, A. Krawciw, S. Lilge, and T. D. Barfoot, "Radar teach and repeat: Architecture and initial field testing," in *2025 IEEE International Conference on Robotics and Automation (ICRA)*. IEEE, 2025, pp. 13 021–13 027.
- [31] S. Dingler and H. Burrichter, "A visual study of ICP variants for lidar odometry," *arXiv preprint arXiv:2511.14919*, 2025.
- [32] A. Censi, "An ICP variant using a point-to-line metric," in *2008 IEEE international conference on robotics and automation*. Ieee, 2008, pp. 19–25.
- [33] Y. Chen and G. Medioni, "Object modelling by registration of multiple range images," *Image and vision computing*, vol. 10, no. 3, pp. 145–155, 1992.
- [34] A. Segal, D. Haehnel, and S. Thrun, "Generalized-ICP," in *Robotics: science and systems*, vol. 2, no. 4. Seattle, WA, 2009, p. 435.

- [35] G. Agamennoni, S. Fontana, R. Y. Siegwart, and D. G. Sorrenti, "Point clouds registration with probabilistic data association," in *2016 IEEE/RSJ International Conference on Intelligent Robots and Systems (IROS)*. IEEE, 2016, pp. 4092–4098.
- [36] M. Yokozuka, K. Koide, S. Oishi, and A. Banno, "LiTAMIN2: Ultra light lidar-based slam using geometric approximation applied with KL-divergence," in *2021 IEEE international conference on robotics and automation (ICRA)*. IEEE, 2021, pp. 11 619–11 625.
- [37] H. Yang, J. Shi, and L. Carlone, "Teaser: Fast and certifiable point cloud registration," *IEEE Transactions on Robotics*, vol. 37, no. 2, pp. 314–333, 2020.
- [38] A.-R. Dannaoui, J. Laconte, C. Debain, F. Pomerleau, and P. Checchin, "When and where localization fails: An analysis of the iterative closest point in evolving environment," in *2025 European Conference on Mobile Robots (ECMR)*. IEEE, 2025, pp. 1–7.
- [39] L. Carlone, A. Kim, T. Barfoot, D. Cremers, and F. Dellaert, "Slam handbook: From localization and mapping to spatial intelligence," 2025.
- [40] S. Khatkhat, H. Nguyen, F. Mascari, T. Dang, and K. Alexis, "Complementary multi-modal sensor fusion for resilient robot pose estimation in subterranean environments," in *2020 International Conference on Unmanned Aircraft Systems (ICUAS)*. IEEE, 2020, pp. 1024–1029.
- [41] K. Burnett, Y. Wu, D. J. Yoon, A. P. Schoellig, and T. D. Barfoot, "Are We Ready for Radar to Replace Lidar in All-Weather Mapping and Localization?" *IEEE Robotics and Automation Letters*, vol. 7, no. 4, pp. 10 328–10 335, 2022.
- [42] J. Zhang and S. Singh, "Low-drift and Real-time Lidar Odometry and Mapping," *Autonomous Robots*, vol. 41, no. 2, pp. 401 – 416, February 2017.
- [43] T. Shan and B. Englot, "LeGO-LOAM: Lightweight and Ground-Optimized Lidar Odometry and Mapping on Variable Terrain," in *2018 IEEE/RSJ International Conference on Intelligent Robots and Systems (IROS)*, 2018, pp. 4758–4765.
- [44] H. Wang, C. Wang, C.-L. Chen, and L. Xie, "F-LOAM: Fast Lidar Odometry and Mapping," in *2021 IEEE/RSJ International Conference on Intelligent Robots and Systems (IROS)*. IEEE, 2021, pp. 4390–4396.
- [45] J. Behley and C. Stachniss, "Efficient Surfel-Based SLAM using 3D Laser Range Data in Urban Environments," in *Proc. of Robotics: Science and Systems (RSS)*, 2018.
- [46] X. Chen, A. M. E. Palazzolo, P. Giguère, J. Behley, and C. Stachniss, "SuMa++: Efficient lidar-based semantic SLAM," *2019 IEEE/RSJ International Conference on Intelligent Robots and Systems (IROS)*, pp. 4530–4537, 2019. [Online]. Available: <https://api.semanticscholar.org/CorpusID:201035892>
- [47] F. Khameneifar and H. R. Ghorbani, "On the Curvature Estimation for Noisy Point Cloud Data via Local Quadratic Surface Fitting," *Computer-Aided Design and Applications*, 2018.
- [48] D. S. Meek and D. J. Walton, "On surface normal and Gaussian curvature approximations given data sampled from a smooth surface," *Computer Aided Geometric Design*, vol. 17, pp. 521–543, 2000.
- [49] I. Douras and B. F. Buxton, "Three-Dimensional Surface Curvature Estimation using Quadric Surface Patches," in *Scanning Proceedings*, vol. 44, no. 0, 2002.
- [50] R. Liang, "Research on Point Cloud Registration Algorithm Based on Gaussian Curvature," in *2020 35th Youth Academic Annual Conference of Chinese Association of Automation (YAC)*, 2020, pp. 465–471.
- [51] Y. Asao and Y. Ike, "Curvature of point clouds through principal component analysis," 2021, preprint, available online: <https://arxiv.org/abs/2106.09972>.
- [52] B. Behroozpour, P. A. Sandborn, M. C. Wu, and B. E. Boser, "Lidar system architectures and circuits," *IEEE Communications Magazine*, vol. 55, no. 10, pp. 135–142, 2017.
- [53] M. Zhao, J. Wang, T. Gao, C. Xu, and H. Kong, "FMCW-LIO: A doppler lidar-inertial odometry," *IEEE Robotics and Automation Letters*, vol. 9, no. 6, pp. 5727–5734, 2024.
- [54] C. Pang, Z. Shen, R. Wu, and Z. Fang, "Efficient doppler lidar odometry using scan slicing and vehicle kinematics," *IEEE Transactions on Instrumentation and Measurement*, 2024.
- [55] C. Courcelle, D. Baril, F. Pomerleau, and J. Laconte, "On the importance of quantifying visibility for autonomous vehicles under extreme precipitation," *Towards Human-Vehicle Harmonization. De Gruyter*, pp. 239–250, 2023.
- [56] Z. Chen, H. Chen, Y. Qi, S. Zhong, D. Feng, J. Wu, W. Wen, and M. Liu, "RELEAD: Resilient localization with enhanced lidar odometry in adverse environments," in *2024 IEEE International Conference on Robotics and Automation (ICRA)*. IEEE, 2024, pp. 3999–4005.
- [57] X. Zuo, Y. Yang, P. Geneva, J. Lv, Y. Liu, G. Huang, and M. Pollefeys, "LIC-Fusion 2.0: Lidar-inertial-camera odometry with sliding-window plane-feature tracking," in *2020 IEEE/RSJ International Conference on Intelligent Robots and Systems (IROS)*. IEEE, 2020, pp. 5112–5119.
- [58] C. Zheng, W. Xu, Z. Zou, T. Hua, C. Yuan, D. He, B. Zhou, Z. Liu, J. Lin, F. Zhu, *et al.*, "Fast-livo2: Fast, direct lidar-inertial-visual odometry," *IEEE Transactions on Robotics*, 2024.
- [59] S. Boche, J. Jung, S. B. Laina, and S. Leutenegger, "OKVIS2-X: Open keyframe-based visual-inertial slam configurable with dense depth or lidar, and gnss," *IEEE Transactions on Robotics*, 2025.
- [60] P. Pfreundschuh, H. Oleynikova, C. Cadena, R. Siegwart, and O. Andersson, "COIN-LIO: Complementary intensity-augmented lidar inertial odometry," in *2024 IEEE International Conference on Robotics and Automation (ICRA)*. IEEE, 2024, pp. 1730–1737.
- [61] S. Marmaglio, N. N. Hoang, M. Savardi, M. Sgrenzaroli, G. Vassena, and A. Signoroni, "Degeneracy-resilient lidar odometry via reflectance-derived correspondences," 2025.
- [62] N. Chebrolu, T. Läbe, O. Vysotska, J. Behley, and C. Stachniss, "Adaptive robust kernels for non-linear least squares problems," *IEEE Robotics and Automation Letters*, vol. 6, no. 2, pp. 2240–2247, 2021.
- [63] T.-H. Kwok, "DNSS: Dual-normal-space sampling for 3-D ICP registration," *IEEE Transactions on Automation Science and Engineering*, vol. 16, no. 1, pp. 241–252, 2018.
- [64] P. Petracek, K. Alexis, and M. Saska, "RMS: redundancy-minimizing point cloud sampling for real-time pose estimation," *IEEE Robotics and Automation Letters*, vol. 9, no. 6, pp. 5230–5237, 2024.
- [65] I. Vizzo, T. Guadagnino, B. Mersch, L. Wiesmann, J. Behley, and C. Stachniss, "KISS-ICP: In defense of point-to-point icp—simple, accurate, and robust registration if done the right way," *IEEE Robotics and Automation Letters*, vol. 8, no. 2, pp. 1029–1036, 2023.
- [66] K. Liu, W. Wang, R. Tharmarasa, J. Wang, and Y. Zuo, "Ground surface filtering of 3D point clouds based on hybrid regression technique," *Ieee Access*, vol. 7, pp. 23 270–23 284, 2019.
- [67] A. Paigwar, Ö. Erkent, D. Sierra-Gonzalez, and C. Laugier, "Gnd-Net: Fast ground plane estimation and point cloud segmentation for autonomous vehicles," in *2020 IEEE/RSJ international conference on intelligent robots and systems (IROS)*. IEEE, 2020, pp. 2150–2156.
- [68] N. Qin, W. Tan, L. Ma, D. Zhang, H. Guan, and J. Li, "Deep learning for filtering the ground from ALS point clouds: A dataset, evaluations and issues," *ISPRS Journal of Photogrammetry and Remote Sensing*, vol. 202, pp. 246–261, 2023.
- [69] P. Zeng, A. Presta, J. Reinis, D. Bharadia, H. Qiu, and P. Cosman, "Can we remove the ground? obstacle-aware point cloud compression for remote object detection," *arXiv preprint arXiv:2410.00582*, 2024.
- [70] A. H. Lang, S. Vora, H. Caesar, L. Zhou, J. Yang, and O. Beijbom, "PointPillars: Fast encoders for object detection from point clouds," in *Proceedings of the IEEE/CVF conference on computer vision and pattern recognition*, 2019, pp. 12 697–12 705.
- [71] H. Kim, S. Song, and H. Myung, "GP-ICP: Ground plane ICP for mobile robots," *IEEE Access*, vol. 7, pp. 76 599–76 610, 2019.
- [72] W. Wen and L.-T. Hsu, "AGPC-SLAM: Absolute ground plane constrained 3d lidar SLAM," *NAVIGATION: Journal of the Institute of Navigation*, vol. 69, no. 3, 2022.
- [73] NASA, Apollo Journals, "John's Station 1 Pan South," April 1972, <https://apollojournals.org/alsj/a16/a16pan18425-32emj.jpg>, last accessed on 2026-02-05.
- [74] NASA Science, "Perseverance's Three Forks Sample Depot Selfie," January 2023, <https://science.nasa.gov/resource/perseverances-three-forks-sample-depot-selfie/>, last accessed on 2026-02-05.
- [75] A. Hinduja, B.-J. Ho, and M. Kaess, "Degeneracy-aware factors with applications to underwater slam," in *2019 IEEE/RSJ International Conference on Intelligent Robots and Systems (IROS)*. IEEE, 2019, pp. 1293–1299.
- [76] X. Bai, W. Wen, and L.-T. Hsu, "Degeneration-aware outlier mitigation for visual inertial integrated navigation system in urban canyons," *IEEE Transactions on Instrumentation and Measurement*, vol. 70, pp. 1–15, 2021.
- [77] J. Lee, R. Komatsu, M. Shinozaki, T. Kitajima, H. Asama, Q. An, and A. Yamashita, "Switch-SLAM: Switching-based lidar-inertial-visual SLAM for degenerate environments," *IEEE Robotics and Automation Letters*, vol. 9, no. 8, pp. 7270–7277, 2024.
- [78] G. Yao, H. Wang, and Q. Chang, "D2-LIO: Enhanced optimization for lidar-imu odometry considering directional degeneracy," *arXiv preprint arXiv:2508.14355*, 2025.
- [79] D. Lee, H. Lim, and S. Han, "GenZ-ICP: Generalizable and degeneracy-robust lidar odometry using an adaptive weighting," *IEEE Robotics and Automation Letters*, 2024.

- [80] T. Tuna, J. Nubert, Y. Nava, S. Khattak, and M. Hutter, "X-ICP: Localizability-aware lidar registration for robust localization in extreme environments," *IEEE Transactions on Robotics*, vol. 40, pp. 452–471, 2023.
- [81] T. D. Barfoot, C. H. Tong, and S. Särkkä, "Batch continuous-time trajectory estimation as exactly sparse gaussian process regression." in *Robotics: Science and Systems*, vol. 10. Citeseer, 2014, pp. 1–10.
- [82] T. D. Barfoot, *State estimation for robotics: Second edition*. Cambridge University Press, 2024.
- [83] S. W. Anderson, *Batch continuous-time trajectory estimation*. University of Toronto, 2017.
- [84] Z. Liu and F. Zhang, "BALM: Bundle adjustment for lidar mapping," *IEEE Robotics and Automation Letters*, vol. 6, no. 2, pp. 3184–3191, 2021.
- [85] F. Dellaert and M. Kaess, "Square root SAM: Simultaneous localization and mapping via square root information smoothing," *The International Journal of Robotics Research*, vol. 25, no. 12, pp. 1181–1203, 2006.
- [86] K. MacTavish and T. D. Barfoot, "At all costs: A comparison of robust cost functions for camera correspondence outliers," in *2015 12th conference on computer and robot vision*. IEEE, 2015, pp. 62–69.
- [87] T. D. Barfoot and P. T. Furgale, "Associating Uncertainty With Three-Dimensional Poses for Use in Estimation Problems," *IEEE Transactions on Robotics*, vol. 30, no. 3, pp. 679–693, 2014.